Quantifying Dermatology: Method and Device for User-Independent Ultrasound Measurement of Skin Thickness

by

Judith Michelle Beaudoin

B.S. in Mechanical Engineering
University of Maryland, 2014

Submitted to the Department of Mechanical Engineering
in partial fulfillment of the requirements for the degree of
Master of Science in Mechanical Engineering

at the

MASSACHUSETTS INSTITUTE OF TECHNOLOGY

September 2018

Signature redacted

Author.....
Department of Mechanical Engineering
August 8, 2018

Signature redacted

Certified by.....
Brian W. Anthony
Principal Research Scientist, Department of Mechanical Engineering
Thesis Supervisor

Signature redacted

Accepted by.....
Rohan Abeyaratne
Professor of Mechanical Engineering
Chairman, Department Committee on Graduate Theses

Quantifying Dermatology: Method and Device for User-Independent Ultrasound Measurement of Skin Thickness

by

Judith Michelle Beaudoin

Submitted to the Department of Mechanical Engineering
on August 8, 2018 in Partial Fulfillment of the
Requirements for the Degree of Master of Science in
Mechanical Engineering

ABSTRACT

The research summarized here consists of the design of a device and processing technique to acquire and construct 3D volumetric ultrasound data of the hand and arm. The Repeated Skin Thickness Measurement (RSTM) Device moves a high frequency ultrasound probe linearly in 3 axes in a water tank and images a submerged arm. These images are combined into an ultrasound volume, the skin layer segmented, and the thickness extracted. One particular application is measuring progression of scleroderma, a skin thickening disease. Current measurement techniques for scleroderma progression rely on subjective clinical opinion, lack quantitative rigor, are invasive, and often measure parameters besides thickness that are less closely linked to the progression of scleroderma. The current diagnostic process assesses skin thickness based on a single ultrasound image taken by a user holding the ultrasound probe. The imagery that results from the instrumentation and analysis in this thesis is used to create objective maps of skin thickness to quantify the progression of skin-thickening diseases, and can also be used to observe tendons, ligaments, and the other soft tissue structures of the hand. By examining thickness over the surface of the hand and arm, a more robust metric of progression of scleroderma and other soft tissue disease can be attained.

Thesis Supervisor: Brian W. Anthony
Title: Principal Research Scientist, Department of Mechanical Engineering

ACKNOWLEDGEMENTS

I am immensely grateful to all of the Device Realization Laboratory for their support on this project. First, of course, thank you to Dr. Brian Anthony for the opportunity to discover and work on such an interesting problem, and for his guidance along the way. This thesis would have been impossible without the support, knowledge, and encouragement of my many lab mates. Particular thanks go to Anne Pigula Tresansky for her image processing knowledge and pursuit of doing good science, Rebecca Zubajlo for her clinical expertise and willingness to help navigate the maze of resources at MIT and MGH, Alex Benjamin for his ready ideas to solve any problem, and Ina Kundu Benjamin and Xian Du for their work on skin, which paved the way for this research.

The machine design of this thesis would have been severely lacking without Hilary Johnson, who selflessly and enthusiastically passes on all the good things she has learned. Thank you for your design reviews, your thoughtful thesis edits, our runs by the river, and your bustling expertise.

Outside of lab, I've also loved my time at MIT. Thank you to the many friends who have shared coffee hour, MEGAwomen events, Bible studies, and climbing adventures. Thank you to Leslie and her office, for having the fix to every problem and making my experience in MechE amazing.

This thesis was written during a whirlwind of a year, and its completion was only possible with the support and encouragement of my friends and family, spread across the country. I am so very grateful for all of you. Special thanks to Mercedes for her constant prayers, reassurance, planning help, and friendship. I would not be the engineer or person I am today without my parents, Ron and Betty, and my sister Katie. Thank you for raising me to ask questions, to look for ways to contribute to the greater good, and always to take care of my units. Finally, thank you to Cory, my husband, for your love, your unfailing belief in my abilities, and the adventures we've shared.

CONTENTS

NOMENCLATURE

ABS	Acrylonitrile butadiene styrene
BCC	Basal Cell Carcinoma
CNC	Computer numerical control
CT	Computed tomography
DICOM	Digital Imaging and Communications in Medicine
HFUS	High frequency ultrasound
HF	Hidradenitis suppurativa
LoSSI	Localized Scleroderma Skin Severity Index
MRI	Magnetic Resonance Imaging
mRSS	Modified Rodnan Skin Score
OCT	Optical coherence tomography
PVC	Polyvinyl chloride
RSTM Device	Repeatable Skin Thickness Measurement Device
US	Ultrasound

FIGURES

TABLES

CHAPTER

1

INTRODUCTION

Medicine is in the midst of a push for evidence-based diagnosis and treatment. Rather than relying solely on doctors' intuition or prior experience, the health care industry is seeking to create a standard of clearly documented empirical evidence to establish standards of care [1]. In order to achieve this goal, researchers and doctors must clearly define objective measures to quantify the symptoms and effects of the medical conditions that they desire to treat. Medical professionals may characterize a patient's current physical state with tests of various samples (e.g. blood and other bodily fluids, biopsies), vital signs, and measures of physical capability. Medical imaging, when performed in a controlled manner, may be used to obtain objective evidence below the surface. It allows a clinician to measure the size, material properties, and function (through blood flow and other measures) of bone, veins, muscles, and the many complex systems of the body without invasive surgery. This ability to measure and track medical information safely and effectively plays an important role in accurate diagnosis and longitudinal tracking of human disease.

1.1 Motivation

The work in this thesis grew out of a particular need for quantified, evidence-based medicine in dermatology. While many dermatologic conditions display on the surface, overreliance on the external presentation alone leads to incomplete understanding of the disease [2]. Dermatology often defines a particular condition entirely by its appearance, rather than an understanding of the pathology or subsurface symptoms. Representative of dermatology's need for quantification, scleroderma initially presents as a thickening of the skin, but causes serious systemic effects in many other organ systems, ending in kidney failure, pulmonary fibrosis, pulmonary arterial hypertension, heart failure, malnutrition, and death [3]. Without an adequate, robust metric of the

progression of the disease, it is difficult to conduct drug trials and to monitor the effectiveness of a course of treatment for a particular patient. This thesis focuses on ultrasound imaging of skin to standardize the documentation of the thickening effects of scleroderma.

Additionally, this thesis draws from one of the broad focuses of the Device Realization Laboratory (DRL): eliminating sonographer dependence to fully leverage ultrasound as a safe and inexpensive method of medical imaging. Ultrasound typically images on a single plane, contrasting with methods like CT and MRI which image an entire volume. Instead of a fully automated scan, a sonographer, or ultrasound technician controls ultrasound probe position and contact force on the skin. Varying pressure deforms the tissue being imaged, and changes the echointensity (brightness) of some structures. Locating the correct plane to image a feature of interest is difficult, and may not be possible to relocalize for a comparison in the future. Operator dependence can be reduced by controlling or measuring the coupling of the probe with the skin, through force control [4], force measurement [5], or the elimination of a pressure-based contract by coupling through water [6]. Additionally, the position of the probe can be controlled [6] or tracked [7].

1.2 Approach

This thesis documents the development and testing of a prototype device with controlled translation of an ultrasound probe and water coupling. A precision machine design approach was used, defining functional requirements for the system, and allowing the requirements to drive the strategy selection and design process. The Repeatable Skin Thickness Measurement (RSTM) Device is used to create a fully automated ultrasound volume of the hand and arm to remove the effects of varied probe force. The data acquired is analyzed with an automatic image segmentation process to extract and measure the thickness of the epidermal and dermal layers. Together, the RSTM Device and analytical process provide a large area measurement of skin thickness to quantify the progression of scleroderma. Through a large sampling area and sonographer independence, this ultrasound measurement of skin thickness will be more robust to document smaller variations in skin thickness over time, not just the presence or lack of disease. Small changes in thickness may be unobservable on the surface but may better characterize the progression or improvement of dermatological disease. The result also represents a fully automated volumetric ultrasound scan of the hand which could be used for diagnostic imaging of tendons,

ligaments, and bone surfaces, which are densely populated in the hands. High frequency, high resolution volumetric ultrasound of the hand is potentially useful for wide ranging clinical application.

CHAPTER

2

LITERATURE REVIEW AND PRIOR ART

2.1 Pathology of Scleroderma

Systemic scleroderma is a disease which presents initially as a thickening and hardening of the fingertips, progressing down the arms, and continuing on to have systemic effects in the rest of the body [8]. This has been shown to be caused by an overproduction of collagen in the epidermis and dermis [9]. The overproduction of collagen, which in a healthy individual contributes to the elasticity of the skin and other tissues, in patients with scleroderma creates stiff, thickened tissues [9]. In the skin, this results in reduced mobility and degrades quality of life, while in other organs, including the digestive and repertory systems, its effects can cause organ failure and death [8]. Systemic scleroderma has no cure [8], and the development of effective treatments is further hindered by the lack of objective measures of the disease progression.

2.2 State of the Art for Measuring Scleroderma

The state of the art provides context for the development of a new method of quantifying the skin-thickening effects of scleroderma. We summarize the performance of the current methods based on the following characteristics of an effective quantitative metric [10]. Table 2.1 shows the summary of this evaluation.

1. Quantifiable – identifies quantitative changes from normal, healthy cases
2. Valid - measures what it claims to measure, matches established gold standard
3. Reproducible – maintains interrater reliability
4. Responsive - detects clinical change
5. Feasible – can be implemented inexpensively and safely, is widely available

There is some difficulty evaluating validity, because there is not a consensus on a gold standard for scleroderma severity. In medicine, the gold standard refers to the clinically accepted, best available test with closest results to the ground truth, the actual condition.

Table 2.1: Evaluating the state of the art for scleroderma evaluation

	Quantifiable	Valid	Reproducible	Responsive	Feasible
Clinical scoring	No	Yes	Yes	Yes	No external resources
Punch biopsy*	Yes	Questioned	No	Yes	Lab facilities
X-ray	Yes	More data needed	Yes	Yes	Imaging equipment
Ultrasound	Yes	More data needed	Yes	Yes	Imaging equipment
Durometer	Yes	Non-thickness parameter	Yes	Yes	Small device
Cutometer	Yes	Non-thickness parameter	Yes	Yes	Small device
Elastography	Yes	Non-thickness parameter	Yes	Yes	Imaging equipment

* Current gold standard

The current standard-practice methods consist of various protocols for clinical scoring. These include the Localized Scleroderma (LS) Skin Severity Index (LoSSI), which rates skin condition and a number of set locations and the Manikin method, which measures the percentage of body surface area with clinical involvement [11]. Clinical scoring protocols can achieve interrater reliability above 90% [11], but can only respond to visible changes. These protocols lack truly quantitative metrics and only assess relative severity of scleroderma cases [10]. However, these methods are extremely feasible, both safe and widely available. [11]

Punch biopsies sample skin thickness at isolated locations. While it can capture skin thickness, the biopsy sites create a wound and a risk of infection, while also requiring proper lab facilities to

preserve the sample on a slide and examine it [12]. Additionally, punch biopsies eliminate the ability sample repeatability, due to scarring of the skin. These samples are quite responsive, and are often considered the gold standard [13]. This conclusion is sometimes questioned because the skin can be deformed once removed from the body, and due to the variations possible in the processing of the samples [14].

Outside of punch biopsies, both X-ray and ultrasound imaging can be used for assessing skin thickness [10]. In terms of feasibility, both require imaging equipment which may not be present at a less specialized facility. There are concerns with repeated exposure to X-ray imaging, making it more difficult to compare a healthy baseline of volunteers with adequate sampling. There is also concern as to whether the imaged thickness corresponds to the actual skin thickness, or if imaging distorts the skin boundaries. Answering this question requires continued study beyond comparison to the dubious gold standard of punch biopsy [10]. Despite these doubts, if particular X-ray and ultrasound measures capture the change in skin thickness, it is still clinically useful. When tracking disease progression, the change between measurements is the primary concern, not the absolute thickness.

Durometers are a tool to measure skin hardness. This is a clearly quantitative metric, and their use amounts to a repeatable and feasible process [10] [15]. However, there are doubts as to whether skin hardness, as opposed to skin thickness, is an adequate measure of clinically relevant data [10].

Similarly, a cutometer measures skin elasticity. This gives a quantifiable, repeatable, and feasible metric, but is not widely accepted as responsive to clinical changes and it does not adequately differentiate healthy and sclerotic skin [10][16].

Another method of assessing the mechanical properties of the skin, rather than just its thickness, is shear wave ultrasound elastography [17]. This presents similar challenges to standard ultrasound imaging, feasibility due to equipment access and questions of the validity in the absence of a gold standard, but requires even more specialized equipment. Similar to the durometer and cutometer, more research is required to assess the validity and clinical relevancy of these properties [17].

All of the state-of-the-art measurement methods for scleroderma progression have various deficiencies. Clinical scoring is subjective, biopsies are not repeatable and invasive, and cutometers, durometers, and elastography methods document skin properties that are less fundamentally linked to the progression of scleroderma [10]. X-ray imaging provides an option which is promising, but it has limited feasibility due to exposure to harmful rays. Ultrasound

imaging, while more operator dependent than X-ray imaging, is safer. By reducing operator dependence, and thus increasing the repeatability, this thesis aims to make ultrasound a safe and objective alternative to other scleroderma diagnostic techniques. To further expand the previous work, the following section will outline the uses of ultrasound in dermatology to quantify skin properties and monitor various dermatologic conditions.

2.3 Ultrasound in Dermatology

Dermatology has been slow to employ technologies that quantitatively evaluate progression of dermatologic conditions. Current methods include dermascopes, spectroscopy, OCT, and ultrasound [18]. Dermatologists use high frequency ultrasound (HFUS) in frequencies varying from 10 MHz to 100 MHz, with increased frequency corresponding to increased resolution and decreased depth of imaging. It is a low cost, fast imaging option, particularly suited for assessing the interfaces between tissue types [19]. Dermatologists in some select regions have begun to employ ultrasound as a regular part of practice in dermatology. A study in Spain recorded the use of ultrasound for diagnosis, surgical planning and follow-up for tumors, inflammatory diseases, skin appendages, and cosmetic conditions [20]. The study reported mean patient satisfaction with the procedure as 4.8 on a scale from 0 to 5, as well as an increase in ultrasound use, especially among young dermatologists [20]. This increased use of ultrasound suggests that, given availability of HFUS and adequate dermatologist training, ultrasound imaging can make a positive contribution to the diagnosis and treatment process in dermatology. Applications of ultrasound include B-mode ultrasound of boundaries between tissue types and elucidating details of tissue structure, Doppler ultrasound for conditions with specific venous morphology, ultrasound elastography to determine properties of the skin, and 3D ultrasound reconstructions of various tissues.

2.3.1 B-mode Imaging

Applications for B-mode ultrasound imaging in dermatology are wide-ranging. B-mode imaging provides a quick and relatively cheap method of imaging structures beneath the surface of the skin. 20 to 25 MHz ultrasound shows both the epidermis and dermis, while 50 to 100 MHz ultrasound shows only the epidermis [19]. The clinician should tailor the frequency to the application due to the trade-off between depth of penetration and resolution. Higher ultrasound

frequencies attenuate more quickly, resulting in a lower depth penetration into the tissue, but provide a higher resolution [19]. Generally, dermatologic ultrasound falls between 13.5 and 100 MHz [18]. Lower frequencies from 5 to 12 MHz are used for deeper structures, including subcutaneous tumors and lymph nodes [21]. Table 2.2 shows depth of penetration for various frequencies. The following section will profile the use and success of various frequencies to image skin cancer, scarring, scleroderma, psoriasis, and varying skin structure due to wound healing and aging, particularly focusing on various methods of skin thickness measurement.

Table 2.2: Ultrasound frequency and depth of penetration [22][19]

Ultrasound frequency (MHz)	Approximate depth of penetration (cm)	Resolution (μm)	Visualization
7.5	>4	~210	Subcutis and lymph nodes
13.5-50	3.0-0.3	~158 - 31	Epidermis and dermis
20	0.6-0.7	~72	Epidermis and dermis
50-100	0.3-0.015	~31 - 16	Epidermis only

A large quantity of research in dermatology is concentrated within the application of skin cancer, with a particular concentration on melanoma. Studies used frequencies of ultrasound varying from 10 MHz to 100 MHz to image cancerous lesions. One study used 10 MHz ultrasound to differentiate melanoma thinner and thicker than 1 mm, a benchmark for how deep the incision must be during removal with 86% sensitivity and 95% positive predictive value [23]. Another study found 25 MHz ultrasound more accurate than 930 nm OCT as compared to histopathology for assessing melanoma thickness [24], but is criticized for using too low a frequency of OCT [25]. In contrast, comparing 100 MHz US to 1300 nm OCT (shown in Figure 2.1) found better accuracy with OCT [26]. At this high frequency, only thicknesses less than 1 mm can be assessed, due to the attenuation, necessitating combined methods with optoacoustics and Raman spectroscopy [26]. No studies comparing 20 MHz US to 1300 nm OCT for skin cancer were found; a study on corticosteroid skin thinning found 1300 nm OCT best for assessing the epidermis [27]. 20 MHz US could not distinguish the epidermal layer from the dermis, but better imaged the dermis-subdermal boundary to see the clinical effect of net epidermis and dermal thinning [27].

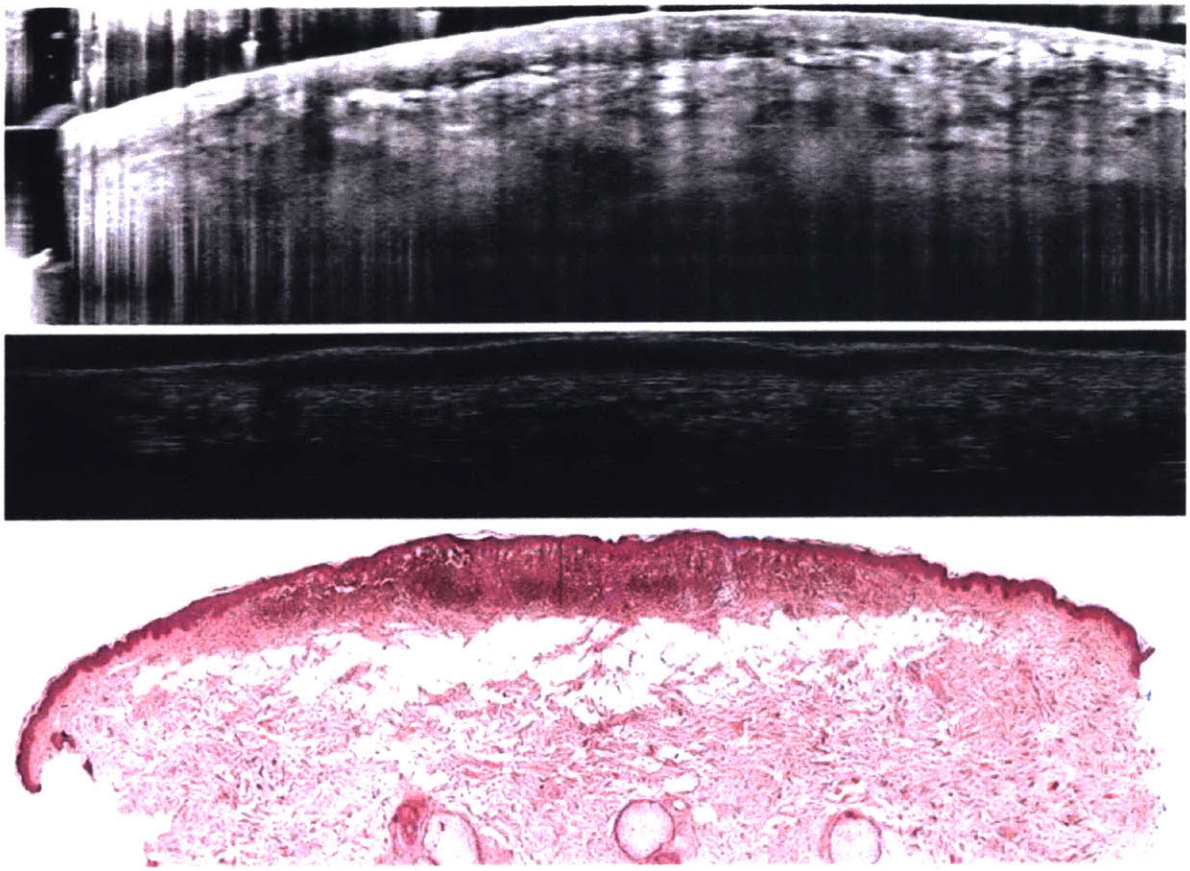

Figure 2.1: Melanocytic nevus imaged with 1300 nm OCT (top), 100 MHz HFUS (middle), and H&E stained histopathology (bottom) [26]

Another approach to cancer identification used an imaging phantom —an object used in medical imaging for calibration or evaluation of imaging equipment — to test the effectiveness of high frequency ultrasound at detecting the presence of micro-tumors, to be applied within the context of Moh's surgery, in which thin layers of skin are progressively removed and tested to achieve clear margins [28]. HFUS successfully demonstrated increased attenuation in areas containing the microbeads used to mimic microtumors [28]. Another study compared HFUS at 40 MHz to the Breslow Index, a measure of tumor penetration with histopathology, concluding it was a useful pre-surgery tool for evaluating locations of tumor margins due to the homogenous hypoechoic appearance of melanoma [29]. Basal cell carcinoma (BCC) was also measured with OCT and HFUS, with 1325 nm OCT more reliable than 20 MHz HFUS compared to histopathology [30]. Some difference may be due to histopathology acquired from a different place than the ultrasound images [30]. In another study measuring BCC with 20 MHz HFUS and OCT, both were found to overestimate thickness compared to histopathology, but OCT was more accurate [31]. Another

tumor type, neurofibroma, located on neurons, was identified with 25 MHz HFUS through the particular spindle shaped hypoechoic areas [32]. The varying conclusions about HFUS's accuracy show the varying abilities of different systems, different doctors, and comparing varying wavelengths in both imaging platforms. When compared to OCT, ultrasound struggles to reveal the same level of epidermal detail due to lower resolution, but it excels when imaging both the dermis and epidermis, while also being generally more usable offering the potential to quickly image larger areas. The focus on tumor thickness in many of these studies continues in the following research on burns, scleroderma, and psoriasis; all these conditions use epidermal and dermal thickness as a marker of disease progression.

The severity of scarring can be assessed by observing increased skin thickness. As with the assessment of cancerous growth thickness, there is disagreement about the precision and accuracy of HFUS for burn thickness measurement. A study on burn thickness in children concluded 8 – 18 MHz HFUS was a reproducible and valid tool compared to a 3D optical reconstruction with multiple camera angles, assessing changes as small as 1 mm [33]. The researchers partially attributed some issues with interrater reliability to relocalizing the area of the scar. The camera approach was also deemed unsatisfactory, due to lack of interrater reliability, so there was no comparison to an accepted measurement [33]. Another study concluded HFUS measurements at 20 MHz was weakly correlated to burn thickness [34]. They attributed problems to insufficient penetration, because the thickened scars sometimes measured 6 to 8 mm to the bottom of the dermis [33]. The study was terminated at n = 10 due to lack of initial correlation, and may have also been confounded by biopsy shrinkage, in addition to the insufficient depth of the ultrasound measurement [33]. A lower frequency ultrasound, 10-15 MHz, also may be more suitable.

As previously discussed, skin thickness is a marker of inflammation and increased collagen production associated with morphea in localized and systemic scleroderma. With a lack of objective measures of scleroderma progression, HFUS has been suggested as a promising option [10] [35]. HFUS at 18 MHz was used to detect the thickened dermis and thinned hypodermis in juvenile localized scleroderma, corresponding to changes in a clinical scoring system, the Modified Rodnan Skin Score (mRSS), found during a clinical drug trial [36]. An 18 MHz probe was also used to detect subclinical involvement in patients with limited cutaneous systemic sclerosis through dermal thickening in areas the mRSS would assess no disease activity [37]. In addition to thickness, there is particular interest in documenting the stage of scleroderma in

particular skin areas. Nazafati et. al. used 14 MHz ultrasound with high reliability to measure dermal thickness, highlighting the 40 mm penetration as ideal for including subdermal involvement, while still distinguishing active disease (hypoechoic), inflammation (isoechoic) and damaged or atrophied areas (hyperechoic) [38]. One element of note is that many of these studies use a very thick layer of ultrasound gel, great than 1 cm, to avoid deformation from normal ultrasound contact forces.

Psoriasis is a common dermatological condition, which presents initially with hardened patches of the skin, called plaques. Skin thickness and blood flow, markers of inflammatory response, can be quantified in psoriasis plaques with ultrasound, both B-mode imaging and Doppler [39]. There is some disagreement about the validity of thickness measurements at different frequencies, with 20 MHz and 40 MHz measuring different values for epidermal thickness [40]. Despite this, both are sensitive to clinical change, noting a decrease in thickness with corticosteroid treatment [40]. Psoriasis also spreads to fingernails, altering blood flow and nail plate structure, also observable with ultrasound, particularly with Doppler greater than 10 MHz [41]. Finally, psoriasis can extend beyond dermatological effects into psoriatic arthritis, which can be observed with HFUS, and differentiated from other types of arthritis [42].

Beyond the various thickness measurements, HFUS is used to assess detailed structure. One application used 20 MHz HFUS of the dorsal and proximal forearm to evaluate photoaging, skin damage caused by sun exposure, with varying echogenicity in the lower and upper dermis, with the total dermis score well correlated to clinical scores of photoaging, and the total dermis score correlated to age at non-photo exposed sites[43]. Another used a 20 MHz focused probe to evaluate tissue change during wound healing, including granular tissue formation and collagen deposition, combining these changes into a quantitative measure of wound healing [44] [45].

2.3.2 3D Ultrasound and Tomography

HFUS imaging can also be implemented to create 3D reconstructions of skin. 3D ultrasound of sebaceous glands using ultrasound microscopy at central frequency 150 MHz has been correlated to skin elasticity as a marker of aging, imaging a patch 4.8 mm square, 1.5 mm deep, reconstructed with 150 B-mode images, using unspecified image processing techniques [46]. 3D reconstructions from 7-15 MHz and 7-18 MHz probes were also found to be useful for monitoring the formation, progression, and healing of hidradenitis suppurativa (HS) sinus tracts, showing tracts and

abscesses not observed in standard observations [47]. HS has been evaluated by measuring the largest cross section of the tract in the transverse plane, but this may introduce operator error [48]. 3D ultrasound is not heavily utilized in dermatology, relatively little investigation has been done into its utility.

2.3.3 Doppler

Doppler ultrasound has been employed in dermatological applications in situations where monitoring blood flow is relevant. Most simply, it can be used to assess the vascularity or nonvascularity of lesions, which can determine malignancy without invasive biopsies [49][50]. Parasitic conditions, like Dermatobia hominis larva, displace the tissue, including blood vessels [51]. Without the usual biopsy or surgery, the presence of larva was confirmed by the hypoechoic rim, hyperechoic center, spontaneous movement, and the peripheral blood flow [51]. It can also be used to characterize fistulous tracts, a key marker in HS [52]. As mentioned in the previous section on psoriasis, it can also be used to characterize blood flow to inflamed regions. These uses all are in the dermis or subdermal, as the epidermis contains no capillaries [53].

2.3.4 Elastography

Another area of imaging in ultrasound is elastography, which measures stiffness of tissue under deformation using compression [29] or shear waves techniques [54]. Its use in the skin is less developed, but some see clinical potential in the assessment of disorders including lower extremity vascular disease, lymphedema, and skin tumors [19]. The application of compression-based elastography is relatively simple, but qualitative. Botar-Jid, et. al., concluded tumor elasticity from real-time elastography using compression was statistically significant, but varied substantially with tumor thickness [29]. Kim et al. measured soft tissue compliance with and without pressure, suggesting a protocol to monitor lymphedema [55]. Soft tissue thickness in healthy subjects was measured using an ultrasound unit with a 7.5 MHz transducer [55]. The image was captured when the thickness of the gel was at least 1 cm and the soft tissue contour was not distorted, then measured with "maximum pressure," at which more pressure did not further thin the tissue [55]. Interrater reliability was "fair to good" in most parts of the arm, but further studies are necessary measuring soft tissue with lymphedema concurrent with treatment [55].

The application of shear wave elastography to the thin layers of the skin is much more complex. Gennisson et al. used a 50 MHz focused transducer surrounded by a vibrating system to generate a 300 Hz shear wave, generating speeds and corresponding stiffness that were corrected for each layer due to refraction biases [54]. The higher frequency (50 MHz) had poor resolution at the muscle- hypodermis boundary [54]. Nguyen et al. created dispersion curves for sub-wavelength layered skin using finite difference modeling with numerically solved boundary conditions to validate shear wave dispersion, comparing their modeling to measurements taken in phantoms yielding less than 1.4% error for dispersion and 5% of speed for elasticity [56]. Xiang et al. did shear wave elastography of various parts of arm using Aixplorer, a 4- to 15-MHz linear probe, which they assert accurately separates epidermal-dermal and dermal-subcutaneous tissue echoes [57]. The study compared measurements to their symmetric counterparts, as well as measured on different axis, yielding good agreement and inter-observer viability, but concluded more validation was needed on both diseased and healthy skin, especially considering variation in age, gender, and handedness [57]. Some studies have been done with diseased skin; Lee et. al. characterized scleroderma skin elasticity with shear wave elastography and acoustic radiation force impulse (ARFI), using a Siemens 14L5 linear array on an ACUSON S2000™ scanner [17]. The speed of sound was 200% higher in sclerotic lesions and 25% higher in patients with morphea compared to healthy patients [17]. Wang et. al. found a significant increase in both thickness and elastic modulus in sclerotic skin in both atrophy and sclerosis assessed with shear wave elastography [58]. Mettler et. al. used an SL15-4 transducer to conduct shear wave elastography, evaluating facial adhesions before, during, and after treatment, guiding the targeted location of treatment and evaluating the outcome, but provided no comparison to evaluate the relative efficacy of the elastography- guided treatment and treatment guided by visual and manual inspection [59]. Ultrasound elastography is still in its infancy in the world of dermatology, and there is the need to unite these clinical applications and controlled testing.

2.3.5 Ultrasound in Hands and Wrists

In addition to outlining the use of ultrasound in dermatology, because this thesis will focus on volumetric ultrasound of the hands and arms, we will examine alternative uses for this imaging system in the hands and arms. As the hands are relatively thin (6.1 cm at thickest for a 99th percentile man [60]), this opens up the opportunity to use HFUS to image other structures of the

hand and wrist, including tendons, ligaments, and nerves. The detailed tendon and ligament structure of the hand provide many opportunities for injury within a relatively small portion of the body. Skiers thumb (a tear in the UCL), trigger finger (a thickening of the synovial sheath and pulley tendon), and some acute pulley tendon injuries (tears frequently associate with rock climbing) can all be imaged with HFUS [61][62]. Diagnosing all these injuries requires careful scanning technique with finger motion and knowledge of anatomical landmarks to correctly identify the structure in question [61]. The thickness of tendons shows psoriatic arthritis involvement, which can be measured with 10-22 MHz US [63]. Carpal tunnel syndrome is visible as deformation of the nerve or tunnel [61]. HFUS is also used to diagnose mass lesions in the hand and identify the presence of foreign bodies [61]. Any hand-specific ultrasound methods would have wide-ranging applications for the many orthopedic and nerve concerns of the complex structure of the hand. Feet have a similar form factor, complexity, and propensity to both overuse and traumatic injury, creating more potential for overlap of methods.

2.4 Prior Art for Fixed-Frame Systems

This thesis focuses on the creation of a constrained ultrasound probe system, imaging a large area of the hand and arm through controlled translation, followed by automatic segmentation of the skin layers in the reconstructed volume. The final aspect of the background is the prior art for the design of similar hardware and software systems controlling the probe position and coupling with water. Most 3D ultrasound is done by either actuating or detecting small motions of a probe, thus constructing a small localized volume, rather than an image over an individual plane, or with a 2D ultrasound array [64]. There are relatively few examples of larger translations of ultrasound elements for volume reconstruction. One application is scanning of a single element or probe around a circular tank, which can be used for imaging extremities, particularly for fitting of prosthetics for amputee [6]. Another clinical need is ultrasound examination of breast tissue for tumors, particularly in dense breasts [65]. The breast can be imaged with a ring or half-hemisphere of ultrasound elements, as done by Delphinus Medical Technologies [66] [67].

2.5 Summary

There is currently a lack of quantifiable, valid, reproducible, responsive, and feasible metrics for the progression of scleroderma. Researchers have used ultrasound measurement in a single location, but the results have not been consistent for longitudinal monitoring. By measuring skin thickness with ultrasound over a larger area, this research builds a more robust quantitative metric. Additionally, ultrasound is underused in the field of dermatology more broadly, and there is an opportunity to innovate in volumetric ultrasound imaging of the skin and other soft tissues of the hand and arm.

CHAPTER

3

SYSTEM DESIGN

3.1 Problem Statement and Goal

In response to the underuse of ultrasound in dermatology and, in particular, the lack of repeatability in positioning for ultrasound measures of skin thickness, this new Repeatable Skin Thickness Measurement (RSTM) Device enables dermatology practitioners to use ultrasound in a repeatable and safe way to obtain larger area measurements of skin thickness. Current ultrasound use relies on a technician to apply the probe, introducing variation due to small changes in probe location and angle. This research designed and tested a device for larger area measurements of skin thickness to enable quantifiable, valid, reproducible, responsive, and feasible data collection in dermatology. By taking distributed ultrasound images over the surface of the arm and hand, this new technique enables comparison between the thickness measurements across the area, forming the basis of a consistent metric to track progression of skin-thickening diseases like scleroderma. By acquiring a full map of skin thickness, we aim to create a more sensitive longitudinal metric of changes in skin thickness in a patient with scleroderma than measurement based on a single ultrasound slice. The RSTM device realizes this goal by integrating three components: a Philips iU22 ultrasound machine, operated at 12 MHz; a machine for actuating and recording probe placement, removing technician error; and image processing software to automatically extract skin thickness.

3.2 Functional Requirements and Design Parameters

This section outlines the functional requirements for the complete imaging system, listed in Table 3.1, including the probe placement mechanisms, the ultrasound machine, and the image processing algorithms. The design and methods chapters to follow detail these components. In

particular, all three components contribute to the accuracy and precision of skin thickness measurement.

Table 3.1: System functional requirements

Functional Requirement	Design Parameter
Precise skin thickness measurement	• Measure skin thickness within 0.25 mm • Apply even pressure to the skin • Record probe placements ± 1 mm
Easy to setup and operate	• Fits within current technician workflow • Less than 5 minutes for setup and calibration per patient
Ergonomic for patient	• Fits x% to xx% male and females • Support arm in natural position
Short test time	• Less than 5 min to minimize motion
Safe	• Do no harm to the patient or operator • Meet IRB protocol

1. Precision of skin thickness measurements

The imaging and thickness extraction must record depth with **0.25 mm** precision. Adult forearm and hand skin averages 1.12 to 1.50 mm for women and 1.31 to 1.5 for men [68]. In the fingers, one study measured normal skin at 1.89 mm thick on average and sclerotic skin 3.17 mm thick [69]. A resolution of 0.25 mm in depth will allow detection of skin thickness changes approximately 20% from normal. To adequately measure skin thickness over a larger area, the probe placement must be recorded within **1 mm** precision. Furthermore, measuring skin thickness within 0.25 mm accuracy requires even, consistent pressure distribution on skin. Pressure on the skin deforms the skin, skewing the results. The imaging technique must apply consistent or no pressure to avoid distorting the skin measurements.

2. Easy set up and tests for operator

A major barrier to the implementation of many new medical devices is the workflow and ease of use for the clinician or medical professional conducting a test or procedure. The device must

not require extensive setup or calibration for each patient, less than 10 minutes, and must be easy to learn to use.

3. **Ergonomic for patient**

Especially due to the reduced mobility of patients with scleroderma or another soft tissue injury or disease in the arm, the scan should provide a comfortable resting position for the patient, to allow them to remain still and reconstruct the volume based on the position of the probe relative to the tank.

4. **Convenient, quick test, less than 5 minutes per arm**

To minimize the effects of motion on the scan, it should take no longer than 5 minutes. Imaging an arm or other extremity is much easier in this respect because of the absence of large scale respiratory or cardiac motions.

5. **Safe**

The device must be safe to patient and operator, meeting IRB protocols.

To accomplish the goal of volumetric skin thickness measurement, the device and analysis need precise information about the skin boundaries relative to each other. The other requirements take into account both users of the device, patient and clinician. A negative experience for either user hobbles implementation of any medical device.

3.3 Strategies and Concepts

To contribute to a method of skin thickness measurement with a larger area of interest, greater than one ultrasound slice, the RSTM Device must identify the relative position of different ultrasound images. There are two main strategies: controlling probe position or sensing and measuring probe position. The first strategy decision was to control the position of the probe because sensing probe position is a non-trivial problem [70], which currently cannot be done precisely enough for the millimeter level measurements needed for meaningful skin thickness measurement. Once this choice was made, a number of strategies were considered to couple the probe with the arm, a thin gel layer with measured or controlled probe force, a thick gel layer, or a tank and water-based approach. In the interest of simplifying the number of variables recorded, a thin gel layer was eliminated, and the tank and water approach chosen primarily for the ease of

CHAPTER

4

DESIGN

4.1 Design Overview

The previous section established the overall functional parameters and some broad, system-level design decisions, particularly a controlled translation of the probe in a water-filled tank. The following section will describe the design of a machine to produce continuous, repeatable, and accurate X and Z, and discrete Y translation. Table 4.1 shows the characteristics of the RSTM Device (design parameters) that satisfy each functional requirement.

Table 4.1: Functional requirements and design parameters

Functional Requirements	Design Parameters for Imaging
Skin thickness measured within **0.25 mm**	• No additional pressure from scanning - water coupling • Resolution of ultrasound (pixels/mm) • Mechanism to move probe in XYZ with appropriate accuracy • Robust coupling between probe and translation mechanism
Easy set up and tests for operator	• Operator actions to collect ultrasound data • Operator actions to move probe • Zeroing procedure
Ergonomic for patient	• Hold arm stationary in level for both dorsal and ventral sides • Meet a range of human factors (1% female to 99% male of human bodies) • Record data from finger tips to elbow • Holds arm in a position that can be maintained comfortably for the duration of the scan

quick probe motion over larger areas and increased user comfort. Because the motion control for the probe provides a known coordinate for each ultrasound image, the series of collected images can be assembled into a volume. The image processing method then uses the volume to evaluate skin thickness along the surface of the hand and arm, by extracting the top and bottom skin boundaries and evaluating the distance between boundaries. The assembled volume can also be viewed along any plane to observe tendons and other soft tissue structures of the hand and arm.

Convenient, quick test, under **5** minutes for an arm	• Speed of motor • Length of ultrasound probe path • Time between ultrasound scans

A two axis gantry system driver by stepper motors was selected to control the translation of the probe. The continuous motion of the X and Z axes was provided by lead screws, and the entire gantry stepped along two rails to produce discrete Y-axis motion. To collect ultrasound data over the area of the tank with the slope of the armrest, the gantry needed 250 mm of travel in the X-axis, 500 mm of travel in the Y axis, and 50 mm of travel in the Z axis. A standard ultrasound probe was coupled to the Z axis and moved by the gantry over the subjects arm in a tank of water. To create repeatable motion, a primary challenge is coupling the probe repeatably to the gantry. The problem of constraining curved objects is discussed in greater detail in the following analysis section. A pseudo-kinematic coupling was used to create the discrete motion in the Y direction. While complicating operator tasks slightly, this allows for a cheaper and simpler prototype machine.

The completed design is shown below in Figure 4.1a, the completed design with labeled components and coordinate system in Figure 4.1b, and the assembled RSTM Device in Figure 4.2. The probe is constrained in a molded socket with an elastic strap (Figure 4.1b, 1). The probe is moved in the X and Z directions by stepper motors in a PVC frame (2, 3). This frame is picked moved in the Y direction by the operator and re-aligned by a pseudo-kinematic coupling of steel bearings and an aluminum frame (4). The subject's arm is constrained against two pins (5) and held on an angled armrest (6), also made of PVC, tilted to allow for comfort even with limited flexibility. This armrest is placed inside a tank (7) which is filled with water as the ultrasound coupling from the probe to the arm.

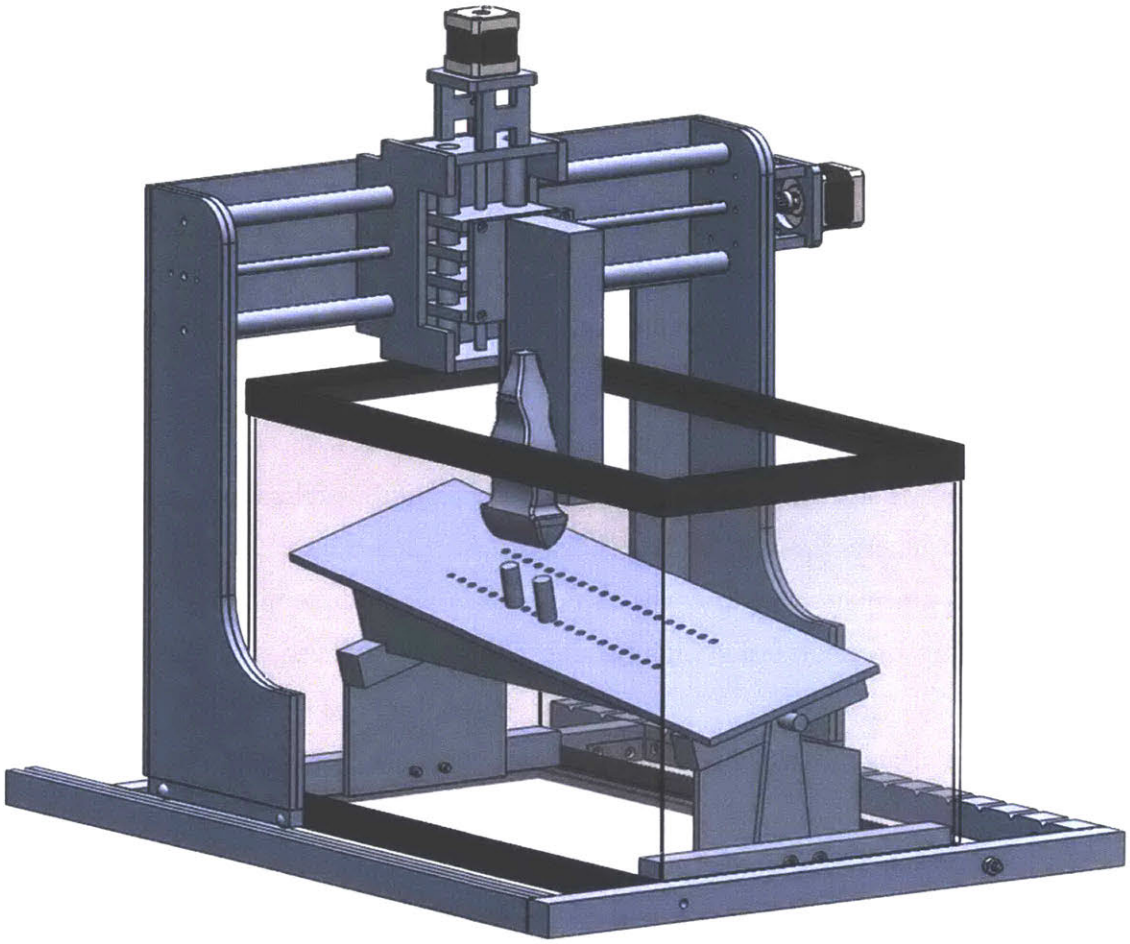

(a)

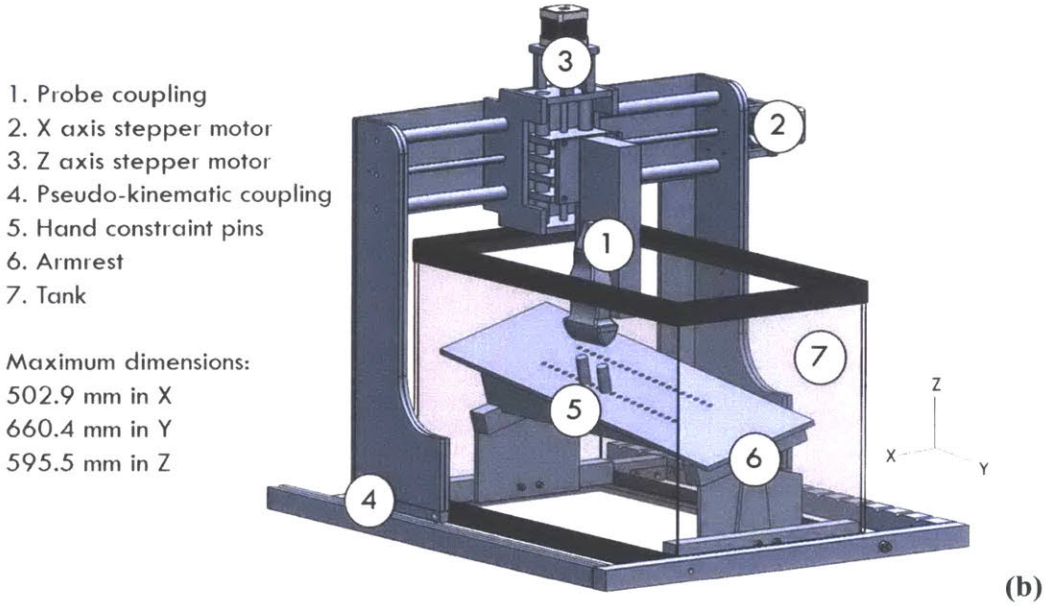

(b)

Figure 4.1: Full assembly (a) with coordinates and labeled components (b)

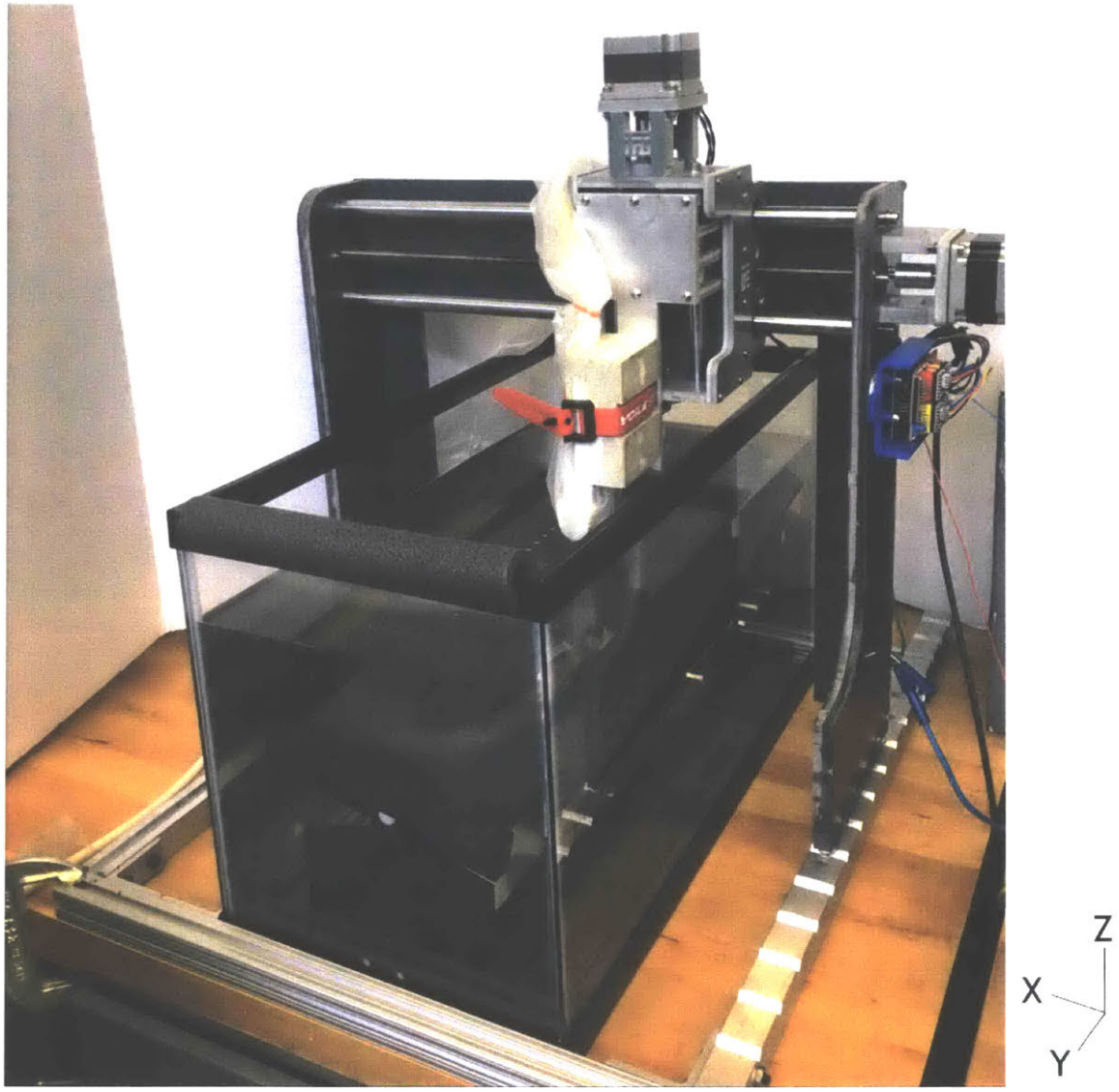

Figure 4.2: Finished RSTM Device

The workflow of scanning with the RSTM Device strives to be simple for both scanning subject and operator. The ultrasound probe is covered with a small amount of gel and a CIV-Flex™ transducer cover, a sterile latex-free tube, closed at the end, which keeps the probe dry. The arm is roughly constrained in the plane with 2 pegs (Figure 4.3) and the gantry lowered and zeroed roughly at the subjects' arm thickness. The scan is conducted by traversing the pseudo-kinematic coupling beginning at the fingertips. For each position of gantry in the pseudo-kinetic coupling, the probe traverses from left to right over the arm, along the X axis, and then the gantry pseudo-kinematic coupling is moved to the next position. This scan pattern, shown in Figure 4.4, covers the entire arm.

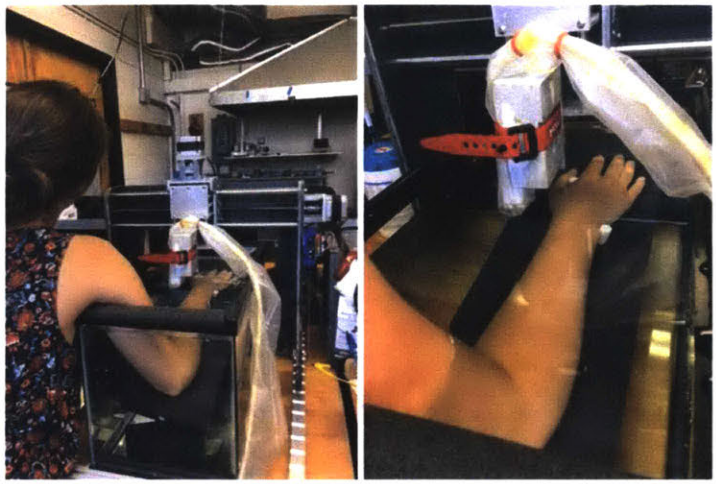

Figure 4.3: Imaging position of the arm. Pegs can be positioned on either side of wrist for comfort

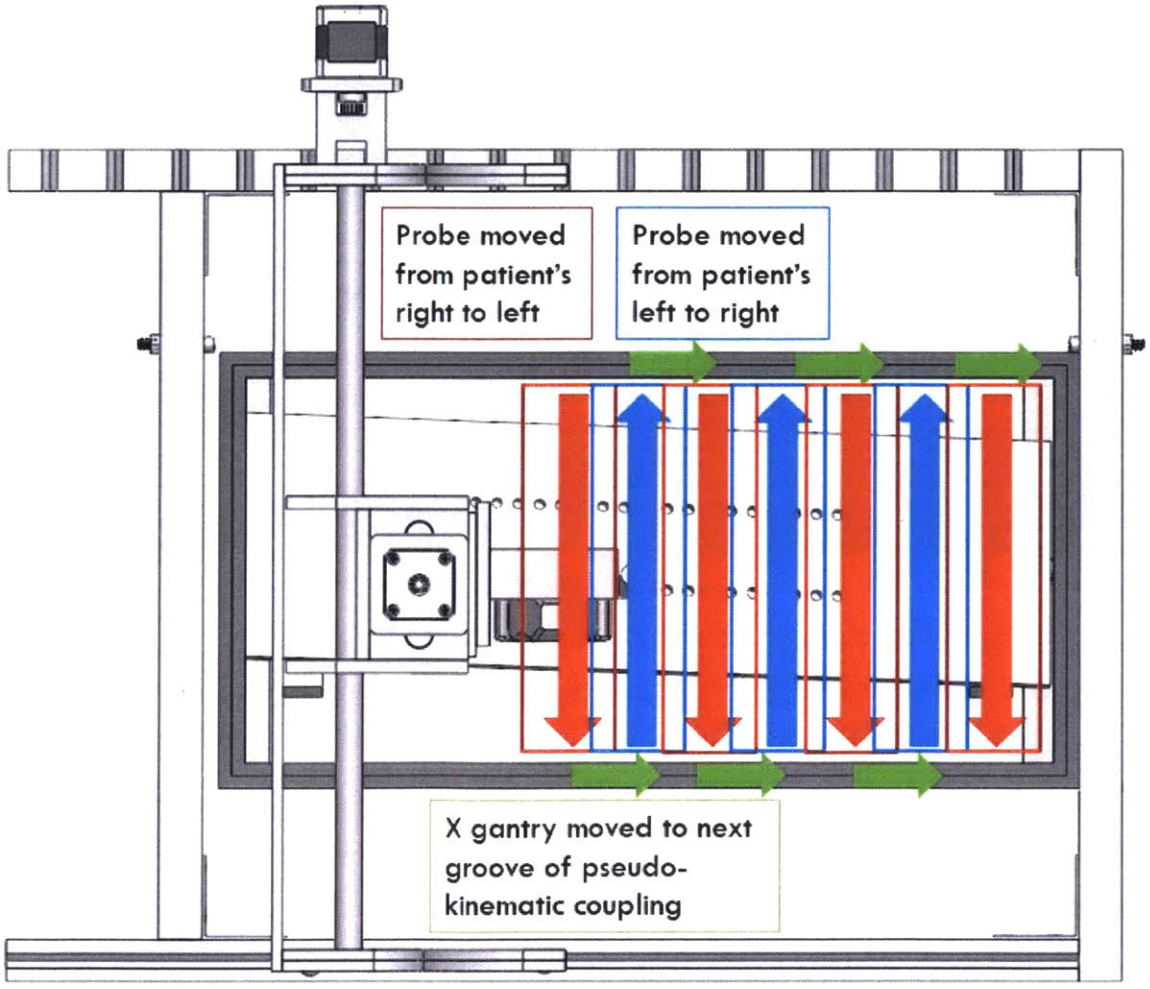

Figure 4.4: Scanning pattern of the probe, red and blue arrows indicating the probe path, green arrows indicate motion between positions of the pseudo-kinematic coupling, red and blue boxes indicated the imaged area

4.2 Design Details

This section will outline the analysis done to determine the couplings, materials choices, and the biomechanics considered in developing the RSTM Device geometry.

4.2.1 Couplings

4.2.1.1 Pseudo-kinematic Coupling

To allow for increased motion along the full length of the arm without a very long leadscrew and additional motors, the gantry needed to move repeatably, but only in discrete positions determined by the width of the probe, along the Y axis. The ultrasound image is 2" wide, so 1.5" increments were required for overlap and complete reconstruction. To accomplish these discrete positions, a kinematic coupling system was designed.

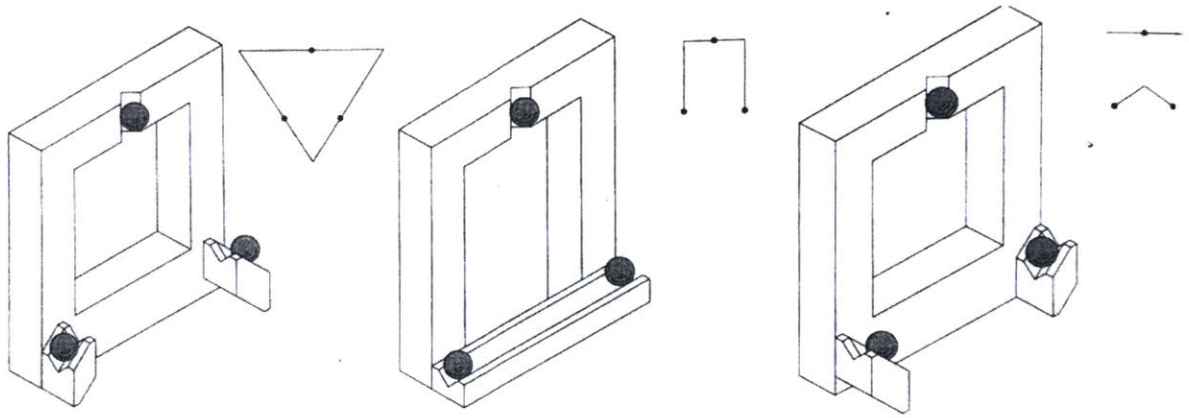

Figure 7.7.4 Different configurations for a kinematic coupling that illustrate how the intersections of the planes containing the contact force vectors can be used to make an assessment of the coupling's stability.

Figure 4.5: Stability of kinematic couplings [71]

A rigid body has 6 degrees of freedom, rotation and translation around each of the 3 axis. Any point of contact constrains one of these degrees of freedom. By producing exactly 6 points on contact, kinematic couplings allow for repeatable positioning of a rigid body [71]. While a typical

kinematic coupling might have 3 radial grooves and spheres at 120°, shown in Figure 4.5 in the most stable configuration, as long as each point of contact restricts an additional degree of freedom, a variety of configurations are possible. Stability is assessed by examining the intersection of the planes containing the contact force vectors, shown to the right of each example in Figure 4.5. For nominal stability, the grooves must be at least at 90° angles, shown in Figure 4.5 in the marginally stable configuration. By placing steel spheres on the bottom of each side of the X carriage, all 6 degrees of freedom, are constrained, shown in Figure 4.6.

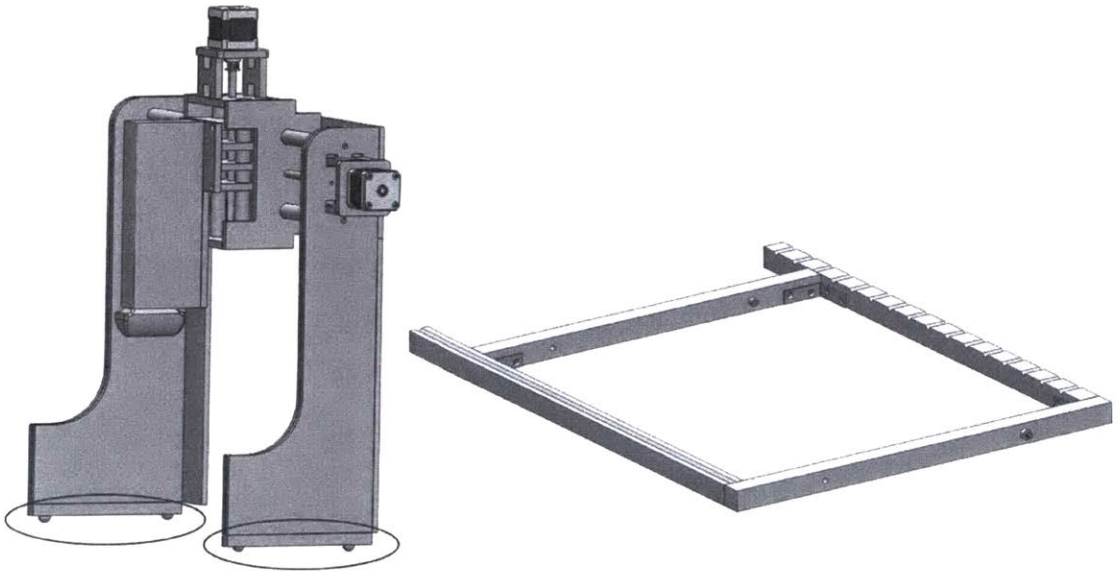

Figure 4.6: KC assembly on CNC frame and base, emphasis on steel spheres

An additional sphere was added to stabilize the assembly, which bears weight only in the case of disturbances, Figure 4.7. This overconstrains the assembly slightly, but still allows for the necessary precision. The groove assembly of marginal stability is acceptable to the very low load on the pseudo-kinematic coupling while the probe is in motion. The coupling is preloaded by the weight of the entire gantry, and only subject to forces from the drag of the water on the probe.

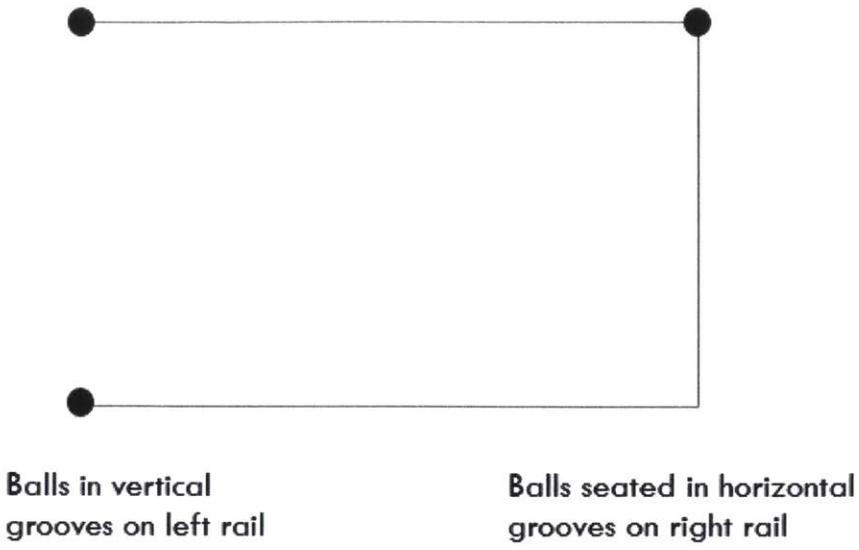

Figure 4.7: Coupling stability of kinematic coupling with 3 balls. A second ball is added in the horizontal grooves (bottom right) for more stability than balancing on a single ball in the center

4.2.1.2 Elastically Averaged Probe Constraint

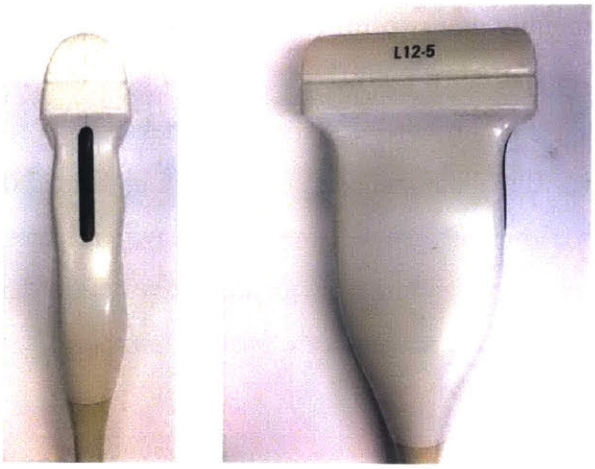

Figure 4.8: Philips iU22 12 MHz probe

The ultrasound probe is designed with ergonomic, curved surfaces, seen in Figure 4.8. This poses a significant challenge to repeatably constrain the probe such that its imaging plane is vertical in the tank. Without flat surfaces, constraining all 6 degrees of freedom cannot be approached with the same 6-point approach described in the previous section on kinematic couplings. For ease of manufacturing, a molded component was made to hold the probe (which operates on the principle of elastic averaging, contact at many points) and the probe is held in place with a polyurethane strap to provide preload, Figure 4.9. This is easily generalizable to most probe shapes, and compatible with the required probe covers for imaging through water. Repeatability of this coupling is described in the

following section on error. The stability, which depends on the subtle curves of the probe, must only withstand the very small drag forces from water, and is sufficient for operation.

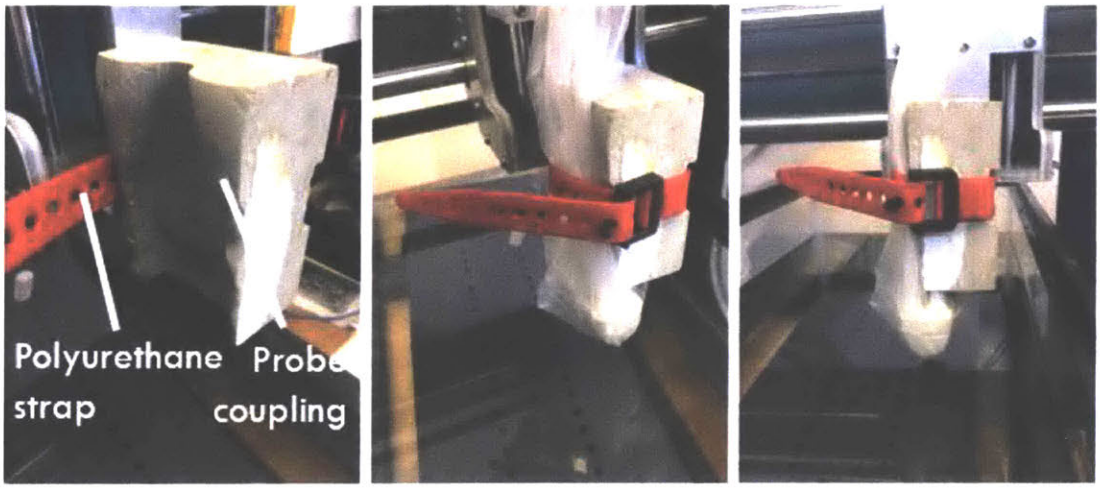

Figure 4.9: Probe coupling in use, without probe (left), an angled view (center), and the operator's view from the side (right)

4.2.2 Material Choices

A number of material choices are worth noting for the particular environment and operation of the RTSM Device. First, the use of metals, particularly any two different metals in water can produce corrosion. Because the arm rest inside the tank does not need to bear large loads, the construction was done entirely in plastic, including 2 widths of PVC sheet and delrin rods for connections. Another important material choice was the kinematic coupling. While high load or repetition applications ideally use ceramic grooves, aluminum grooves were paired with stainless steel balls for ease of manufacturing without the high risk of galling from an aluminum-aluminum pairing [72]. PVC was chosen as a high strength, easily machinable plastic for the frame.

4.2.3 Armrest and Tank Ergonomics

Constraining and accurately imaging arms of a wide variety of sizes requires an adaptable arm rest that constrains the arm both positionally and rotationally, at a set height and slope. As shown by the arrows the Figure 4.10, a person's overall height and arm size both play a role in the optimal imaging position.

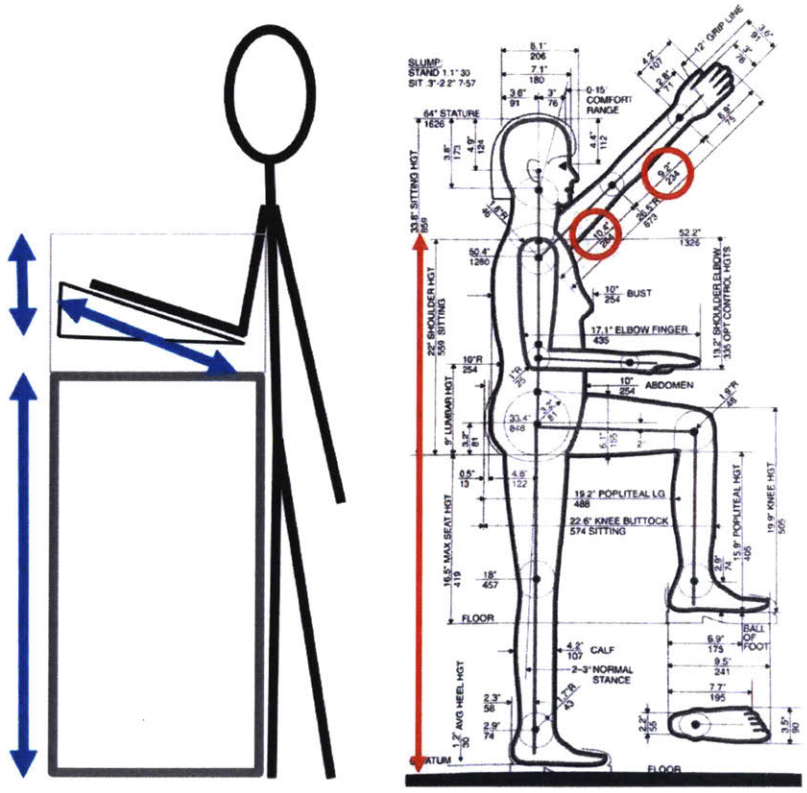

Figure 4.10: Desired imaging position (left) and measurements of 50th percentile woman (right) [60]
The most critical parameters are forearm length, hand length, and hand width, which dictate the imaging space, and upper arm length, which determines whether the elbow reaches the armrest.

Table 4.2 determined the sizes of parts of the armrest and tank.

Table 4.2: Critical dimensions of the RSTM Device with determining physical measurements [60]

Device dimension	Limiting human factor	Measurement
Height from arm rest to top of tank	Length of upper arm of 1% woman	234 mm
Length of an arm rest	Length of forearm and hand of 99% man	487 mm
Distance to furthest peg	99% man forearm + palm	358 mm
Distance between CNC placements	Width of probe image – Philips iU22	51.1 mm
Tilt of armrest from front to back	Thickness of fingertips and palm (see Table 4)	8°
Tilt of armrest from left to right	Balance of flexibility and gravity, experimental	15°

For the best image quality, the probe should be close to the surface of the hand and arm, but never touch it. To avoid the need to change the height of each probe motion in X and Z, the tilt of the armrest was designed to make the upper surface of the arm and hand level. This allows for the same motion in X and Z to be executed at each position of the pseudo-kinematic coupling. By calculating the slope of the palm, the armrest can be sloped at the same angle, as shown in Figure 4.11 and calculated in Table 4.3, converging around 8°.

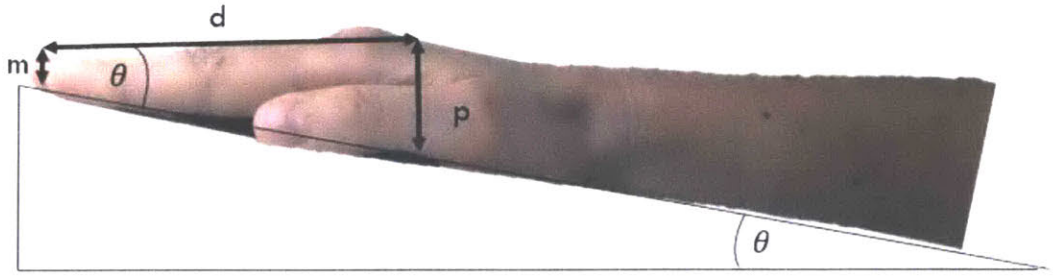

Figure 4.11: Calculating slope of hand

Table 4.3: Determining slope of armrest based on slope of hand [60]

	Percentile	Middle finger thickness (mm) m	Palm thickness (mm) p	Distance finger to palm (mm) d	Angle $\tan^{-1}\frac{p-m}{d}$
Men	99%	19	38	127	8.51°
	50%	16	33	114	8.48°
	1%	13	28	102	8.37°
Women	99%	16	32	114	7.99°
	50%	13	28	101	8.45°
	1%	11	24	89	8.31°

Another ergonomic concern was the ability to place the hand on a horizontal surface comfortably. Because of issues of flexibility for some initial testers, the decision was made to incorporate a rocking mechanism to allow for different slopes for the left and right hand to increase tester comfort. This feature and the assembled armrest in the tank can be seen in Figure 4.12. The two slopes, for imaging clarity and ergonomic comfort are shown below in Figure 4.13.

Figure 4.12: Armrest in tank, tilted to the right for increased comfort

while imaging the dorsal side of the right arm

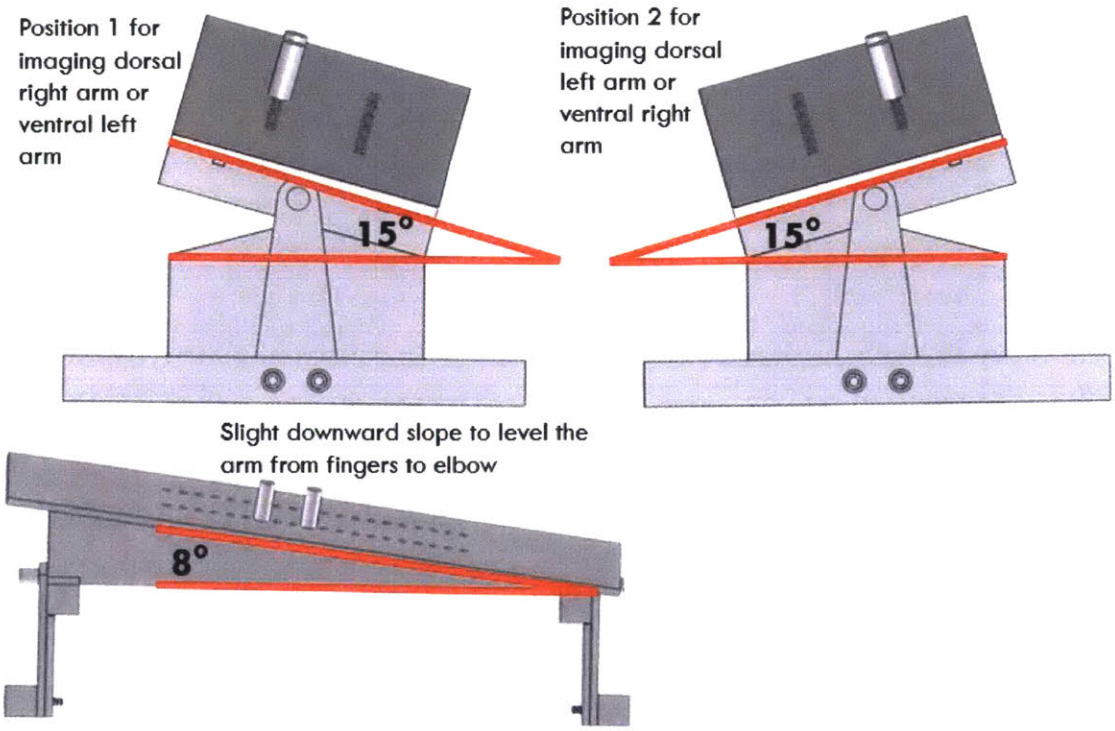

Figure 4.13: Tilt of the armrest in X and Y axes

The hand and arm must be constrained in the plane of the armrest. To exactly constrain an object in a plane, three points of contact are necessary, one for each of the three degrees of freedom (two translational, one rotational). Due to the curved geometry of the hand, this is accomplished by two points of contact from a cylindrical peg between the thumb and index finger, and one point of contact from a cylindrical peg at the at the wrist, shown in Figure 4.14.

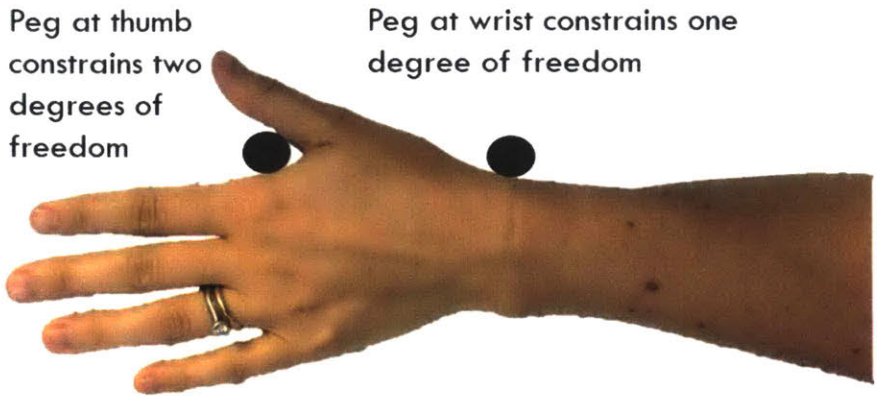

Figure 4.14: Constraint of arm in a plane with two pegs

4.3 Error Budget

The primary goal of probe translation is to obtain reliable skin thickness measurements. The different sources of error in the machine were a critical consideration of the design. Before discussing the cumulative error in the system, it is important to clarify the different frames of reference on the machine, and where precision, accuracy, and repeatability are necessary. Accuracy is the proximity of a measurement to an actual value, while precision, which is necessary for repeatability, is the closeness of a measurement to a prior measurement. There is not any value in repeatability of the probe position between imaging sessions, because the hand is not a rigid body and cannot be repeatably constrained with any particularly high degree of precision,. Within a given imaging session, it is important to know the relationship of one probe position to another probe position, but there is no particular value for accuracy; a constant offset of the probe position will not negatively affect the volume reconstruction or thickness measurements, as long as the proper area is imaged. Because of the insensitivity to a constant offset, the probe coupling repeatability is not highly sensitive. In contrast, the vertical orientation of the probe significantly impacts thickness, and was designed for in the coupling. Due to challenges with accurate stepper motor motion and the ultrasound machine data collection maximum, discussed in the following sections, error of the kinematic coupling in the X direction also has minimal bearing on the final results.

The errors described in Table 4.4 are the motion of the probe, the point of interest. Because the measurement of interest is the skin thickness, we must examine the effect of each of these error motions on skin thickness. For full volume reconstruction, each of the error motions equally

produce error. For thickness measurement, Z error has a different effect from X and Y error. For a flat skin surface, errors in X and Y do not effect skin thickness measurements because the vertical orientation of the probe captures the actual skin thickness in one image. However, errors in Z thickness lead to a miscalculation of the skin slope, increasing the thickness, as shown in Equation (1) and Figure 4.15.

$$\varepsilon_t = t_a - t_i$$

$$\varepsilon_t = t_a - t_a \cos\theta$$

$$\varepsilon_t = t_a(1 - \cos\theta)$$

$$\tan\theta = \frac{\varepsilon Z}{\Delta X}, \cos\theta = \frac{\varepsilon Z}{\sqrt{\Delta X^2 + \varepsilon Z^2}}$$

$$\varepsilon_t = t_a\left(1 - \frac{\varepsilon Z}{\sqrt{\Delta X^2 + \varepsilon Z^2}}\right) \quad (1)$$

Where ε_t is error in thickness, t_a is the actual thickness, t_i is imaged thickness, εZ is the error in the Z position of the probe, θ is the angle created by εZ, and ΔX is the change in X position between images (see Figure 4.15).

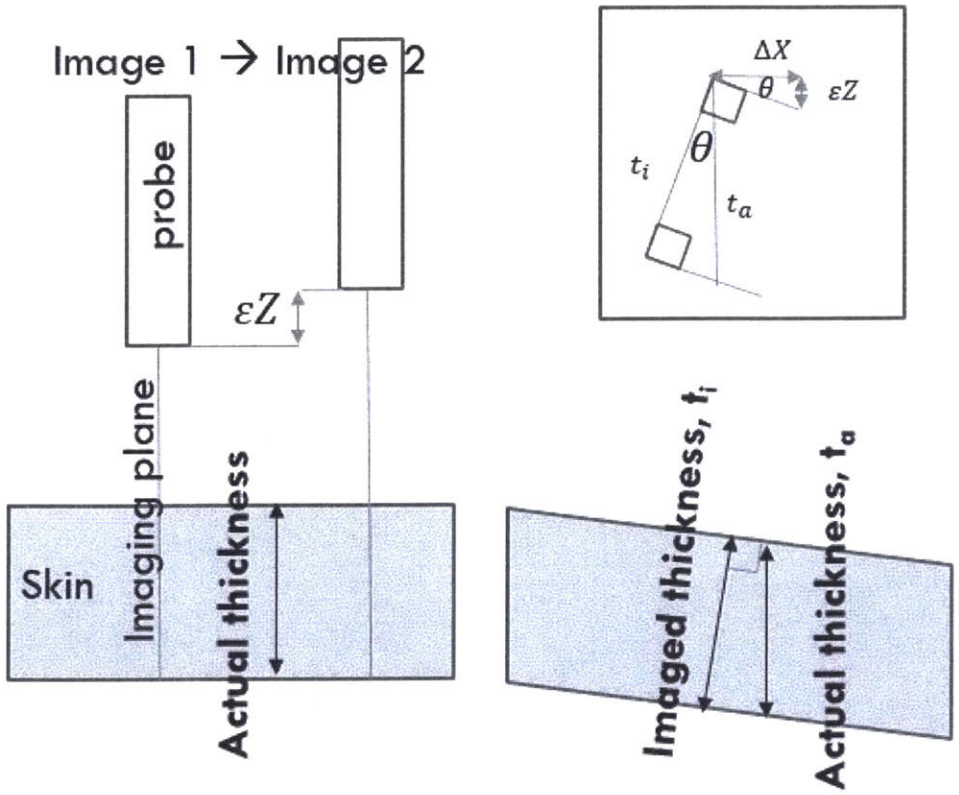

Figure 4.15: Error motion of probe in Z

This error is small for small angles, but shows the increased sensitivity to a lack of Z stability in the machine.

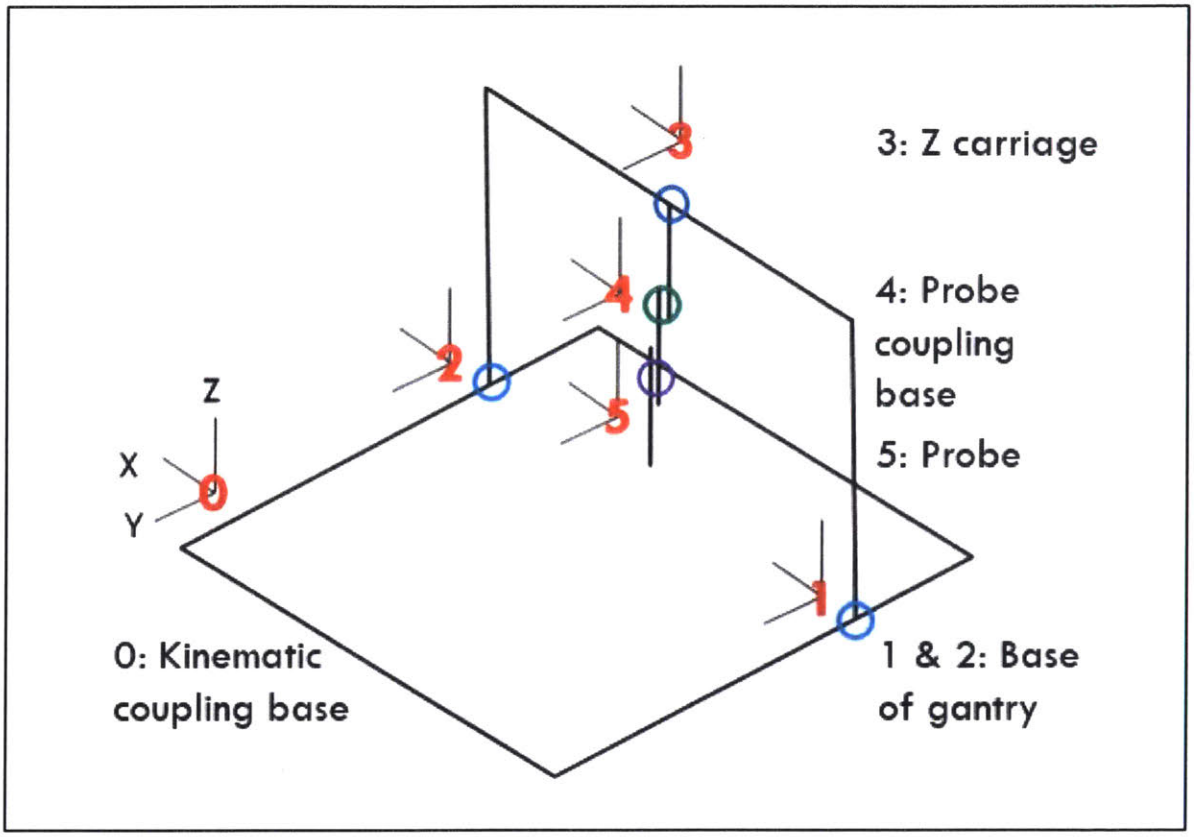

Figure 4.16: Frames of reference for error analysis

After identifying the structural loop and points of connection with coordinate systems, error at each interface along the loop is identified and calculated. Error is present at each of the coupling interfaces (between frames 0-1, 0-2, and 4-5, in Figure 4.16). It is also present in each leadscrew (frames 1-3 and 3-4). The total errors are tabulated in the sensitive directions. The errors can be categorized as geometric, load-induced, thermal, or manufacturing errors. This analysis primarily consists of geometric and load induced deflections, because the machine is stored and operated at room temperature, and manufacturing errors can be corrected during calibration. Table 4.4 summarizes the sources of error in each axis. The total error is tabulated for a given position of the pseudo-kinematic coupling (constant position in Y, while leadscrews move X and Z position), within an imaging session (for one probe coupling iteration), and between imaging sessions (including the errors of all couplings).

Table 4.4: Error analysis

Sources of error	Error Type	Estimation of error	Formula	Error in X (mm)	Error in Y (mm)	Error in Z (mm)
Error in probe coupling	Geometric	Experimental	Maximum error from average in 9 repetitions	0.125	0.126	0.423
Z leadscrew	Geometric	Based on stepper motor accuracy	Error between images, where it will effect thickness	0	0	2.06×10^{-3}
Z assembly deflection	Load induced deflection	Modeled as cantilevered beam deflected by drag force	$\delta = \frac{PL^3}{4EI}$ $I = (r_2{}^4 - r_1{}^4)\frac{\pi}{2}$ $P = F_d = \frac{1}{2}\rho v^2 C_d A$	2.14×10^{-4}	0	0
X leadscrew	Geometric	Based on stepper motor accuracy	error between images (effects thickness)	0	0	2.06×10^{-3}
X leadscrew deflection	Load induced deflection	Modeled as beam fixed/fixed beam	$\delta = \frac{PL^3}{24EI}$ $I = (r_2{}^4 - r_1{}^4)\frac{\pi}{2}$ $P = mg$	3.52×10^{-2}	0	0
Kinematic coupling	Geometric	Experimental	from experiment	0.899	0.922	0.121
Flex in frame	Load induced deflection	Based on experimental flex and worst case geometric analysis	$\delta = L - L\cos\theta$ $\theta = \sin^{-1}\frac{\delta_{flex}}{2L}$	3	0	9.93×10^{-3}
TOTAL - within a given pseudo-kinematic coupling position				0.211	0	4.13×10^{-3}
TOTAL - within a given imaging session				1.11	0.922	0.126
TOTAL – between imaging sessions				4.24	1.05	0.558

The structural deflections are modeled with beam bending, detailed in Appendix A: Error Analysis. The coupling errors are tested experimentally using a laser sight and long distances to quantify

small angular motions. An example setup is shown below in Figure 4.17. The experimental data and calculations are shown in Appendix A: Error Analysis.

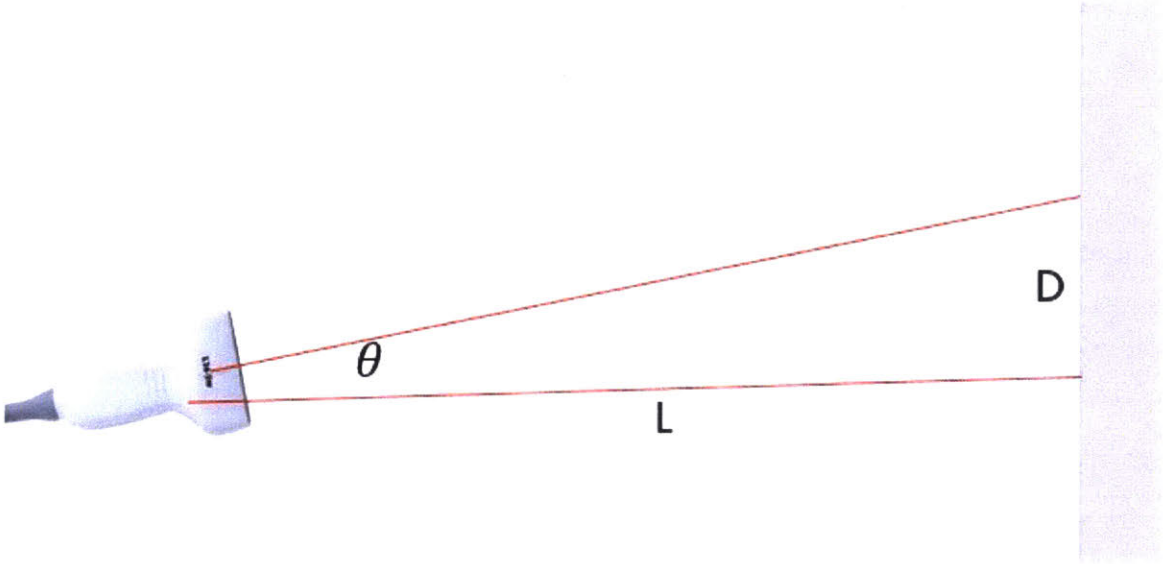

Figure 4.17: Example of laser setup for X-Y error analysis of probe coupling

One source of error which, though unplanned, did not negatively affect the imaging due to challenges with the ultrasound machine, was the effect of flex in the frame on the X positioning of the kinematic coupling. As shown in Figure 4.18, the longer PVC construction allowed for some deformation of the frame when repositioning the pseudo-kinematic coupling. This occurs on the right side, where the pseudo-kinematic coupling grooves do not constrain lateral motion. A maximum of 6 mm of flex was observed on the right kinematic coupling ball, which serves mainly to stabilize the pseudo-kinematic coupling from disturbances. Because the short ultrasound measurements (maximum 10 s) and the lack of encoders, the addition of 2 mm of error in the X direction between ultrasound sweeps is not a problem, due to the alternative alignment methods used in the volume reconstruction, described in

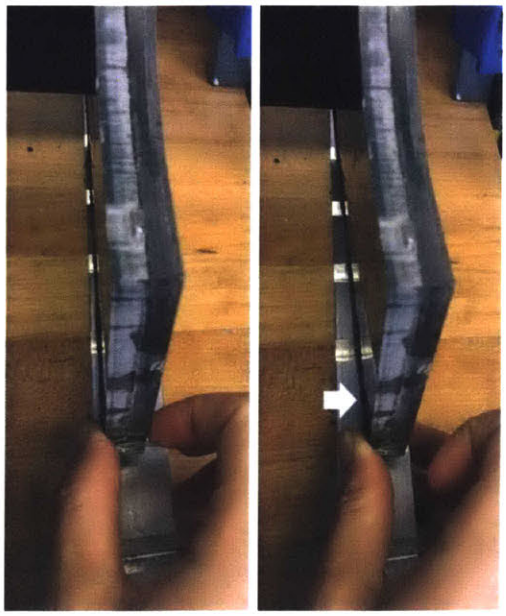

Figure 4.18: Flex in pseudo-kinematic coupling

the following chapter. With longer ultrasound videos and more reliable position sensing, a stiffer, more reliable coupling would become important.

4.4 Manufacturing

A variety of manufacturing processes were used to rebuild the CNC, and fabricate the pseudo-kinematic coupling and probe coupling. While only one RSTM Device was built, care was taken to design for easily manufactured components wherever possible and minimize manufacture complexity.

The new frame of the CNC was fabricated with a Shopbot™ router from 1/4" PVC plastic. The base plate for the probe coupling was waterjet in 1/8" aluminum. The probe coupling was molded from a high density epoxy clay, which allowed for post machining and sanding, while minimizing shrinkage for a tight, reliable coupling. The armrest was cut from the ¼" PVC on the Shopbot™ router, and held together with epoxy [73], and delrin rods. The pegs were 3D printed in ABS on a Stratysus UPrint SE.

Because the kinematic coupling required a higher degree of precision, the seats for the kinematic coupling balls were milled in 1"x1" PVC with a 1.2" ball endmill, and the stainless steel balls epoxied in place. The grooves of the kinematic coupling were milled with a 90° V-groove bit.

CHAPTER

5

METHODS

The following chapter will outline the methods used to gather and analyze the data with the machine described in the previous section. The design of the RSTM Device for probe translation, the methods of the data collection procedures, and the methods used to analyze the data all work together to satisfy the functional requirements detailed in Chapter 3.

5.1 Analysis techniques

The analysis of the gathered data had two goals. The first was to construct an ultrasound volume from the gathered data which can be viewed on any plane. The second was to segment the top and bottom surfaces of the skin, and from this determine the skin thickness over the surface of the arm. This was approached with the following steps:

1. Extract skin surface
2. Align scans and reconstruct volume
3. Extract lower boundary of dermis
4. Determine skin thickness

Due to the limitations of the Philips iU22 ultrasound machine used, the clock of the stepper motors (the location data for the probe) were not synchronized with the internal frame trigger of the ultrasound scanner. Because of this, the extracted skin surface boundary (step 1) is used to align the volumes from neighboring sweeps (step 2).

The development of the particular methods used for the steps involved iterative experiments to determine a sufficiently accurate and computationally accurate method of image processing.

5.1.1 Surface extraction methods and evaluation

The main challenge of the processing is to accurately and quickly segment the skin layer. A number of approaches were considered including active contour methods [74], difference of

Gaussians [75], and various line detection algorithms. The two boundaries, between the water and epidermis, and between the dermis and subcutaneous tissue, provide two different challenges in the different parts of the hand and arm. Figure 5.1 below, shows varying images from the fingers (a) the palm and wrist (b) and the forearm (c). At 12 MHz, skin in the fingers displays primarily as the entry echo. In the arm, there are 2 clearly delineated echoes: the entry level of the epidermis, and a bright line at the bottom of the dermis.

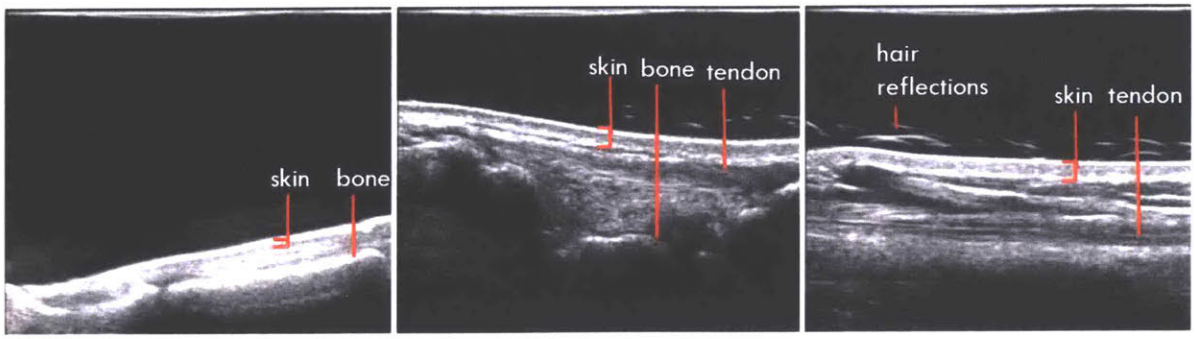

Figure 5.1: 12 MHz ultrasound images showing the skin boundaries seen in the fingers (a), hands (b), and forearm (c)

The skin layer boundaries are detected with two different intensity profiles, as seen in the intensity of the ultrasound slice from top (the source and probe) to the bottom, in the fingers and arm, shown in Figure 5.2.

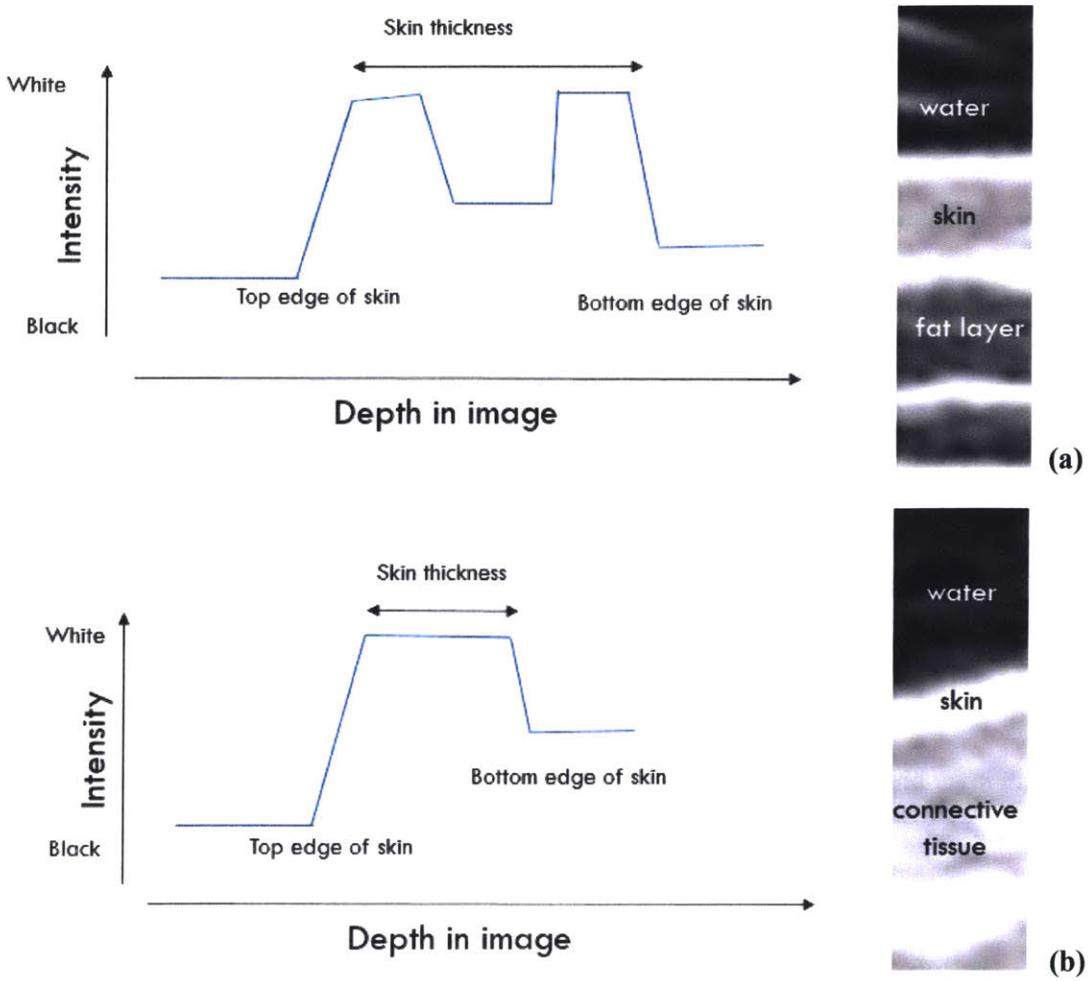

Figure 5.2: Varying imaging intensity profiles typical in the forearm (a) and fingers (b), with sample image of boundary shown at right.

The water-epidermal boundary is quite similar in all parts of the arm. One exception to this case is when the extra reflection is caused by the fine hairs on the dorsal side of the arm (Figure 5.1, c), which complicates the simple increase in the intensity profile. Identifying this boundary could be approached as a line fitting problem, but was deemed too computationally expensive and labor intensive due to the number of images, each with different boundaries to be seeded. With two ultrasound sweeps per pseudo-kinematic coupling, at 10 s per sweep and sampling at 28 Hz, a typical arm has 18 ultrasound sweeps for 100,800 total images. Because the intensity profile looks similar in each column (as displayed in Figure 5.1 and explained in Figure 5.2), which can be

processed with less computationally costly array manipulations, line fitting and other approaches were rejected for the relatively speedy assessment of the gradient with thresholds and intensity.

The second boundary of the skin, the boundary between the dermis and subcutaneous tissue, is much more challenging to extract. Water and the epidermis maintain the same characteristics over the entire arm, and thus produce a similar boundary, which is relatively easy to detect. Subcutaneous tissue, however, can be made up of fat, tendons and ligaments, or muscle. The variation between these materials, in addition to reflections from bones that are close to the surface, leads to variation in the intensity profile in different parts of the arm. Despite these challenges, a relatively simple technique was chosen to allow for quick processing. Using the minimum gradient within a given range, the bottom surface of the skin is extracted well in some samples and with some errors in other samples (Figure 5.3). Further refinement of this processing technique is included in the future work section.

Figure 5.3: Example of extraction of second layer of skin in palm (left) and finger (right)

5.1.2 Parameter selection

An important portion of the development of all the procedures and analysis is the identification, manipulation, and setting of all variables in the processes. For the reader's convenience, these are all profiled below in Table 5.1.

Table 5.1: Parameters for data collection and analysis

	Importance	Final value
Operation of machine		
Scanning speed	Must be fast enough to cover area necessary in 10 s sampling time, but slow enough for sufficient sampling frequency	400 mm/min
Depth	Sufficient to capture relevant data	5 cm
Focal height	The average height of the skin over the surface of the arm while angled on the armrest.	Adjusted for each subject
Skin surface		
Crop from top	Dictates position of probe relative the highest point on hand and arm, too large removes the top skin layer, too small increases false detections from debris	Typically 10-30 pixels
Threshold for location of top edge of skin	Higher thresholds create gaps, lower thresholds create false detections	75 (intensity)
Range to look for max gradient	Too small a range eliminates the need for both threshold and gradient detection, too large leads to erroneous detections of bone	20 pixels
Minimum relevant gradient	Too high a value eliminates detection of less focused skin, too low a value creates false detections due to bubbles or debris	10 intensity/pixel
Range to look for minimum gradient	Minimum skin thickness, too thin will detect the other side of entry echo, too thick will miss thinner skin	From 7 pixels below to 20-50 pixels below the first detected layer
Maximum relevant gradient	Too low a value eliminates detection of less distinct boundaries, too high a value creates false detections	0 intensity/pixel
Outlier elimination sample	Smooth from irrelevant detections without artificially smoothing	25 pixels
Median filter size	Remove irrelevant detections without artificially smoothing	5 pixels

5.2 Final methods

5.2.1 Important imaging characteristics and effect on data collection procedures

A number of precautions in imaging allow for the automatic extraction of the volume of the arm. The primary aim of the following steps is to create a strong, clearly focused entry echo along the surface of the arm. In order to avoid direct contact between the probe and the subject while imaging, the probe must maintain a distance of about 0.25 to 0.5 cm from the highest portion of the hand, while the hand is angled on the armrest. This point typically occurs at the second or third knuckle from the thumb on the dorsal side, or at the pad of the thumb on the ventral side. The proper clearance is achieved by moving the probe over the center of the arm, and using a zeroing tool, which sets the probe 0.25 cm from the surface of the hand at the point nearest contact.

Before the probe is attached, smooth the surface of the probe cover to leave a minimally thick layer of gel between the probe and cover. Wrinkles in the probe cover will create errors in detection, and large amounts of gel will attenuate the ultrasound. The probe is focused on the surface of the skin, and any bubbles displaced from the surface of the skin. The depth of the probe should be set to 4 cm to capture the entire skin surface.

5.2.2 Imaging procedure

The following is a brief description of the operator workflow. For complete instructions, please see Appendix B: Data Gathering Procedures.

1. Power up the CNC and plug the Arduino in to the computer.
2. Power up the ultrasound machine and input patient data.
3. Start Universal GCode Sender, and confirm the paths are set correctly.
4. Position the armrest for the view of the arm to be used for the first scan. Move the probe holder to the center of the armrest.
5. Instruct the subject to place their hand on the armrest, positioning the pegs for maximum comfort and compliance. Move the CNC over their arm's highest point when angled, around their third knuckle (dorsal imaging) or thumb pad (ventral imaging)
6. Place the zeroing tool on the probe holder, and lower it incrementally until just touching the surface of the arm. Set the current position with the values for the center of the path.
7. Allow the subject to move their arm, constrain the probe in the probe holder.

8. Instruct the subject to place their arm and hold still. Begin scanning from the back right, and continue scanning until the upper arm creates a barrier. Record the approximate location of each scan on the arm using the worksheet
9. Allow the subject to relax and remove and dry their arm. Export and save all data.

5.2.3 Image segmentation, volume creation, and thickness measurement

Once the DICOM files are collected and uploaded, the surface of the skin must be extracted.

1. Load DICOM files.
2. Crop, convert to black and white with the luminance component of the YUV color space, and mask measurement bar on the right side
3. Detect the first layer, in each column/
    a. Find location of maximum gradient in each column
    b. Starting 7 – 50 pixels from the top, find the first crossing of the threshold 75.
    c. Average the two numbers in (a) and (b). If the threshold is never crossed or if the maximum gradient is less than 10, the layer is set on the bottom of the image
4. Detect the second layer, in each column
    a. Find the minimum gradient, starting 7 pixels below the first layer, and ending a tunable expected thickness value (typically 20-50 pixels) below the first layer
    b. If the first layer is at the very bottom of the image, set the second layer to the same level. Otherwise, average the two numbers in (a) and (b)
5. Combine any scans that are made during the same Y position of the gantry, due to the 10 second scan limit
6. Smooth surface with median filter (5 pixels squared) and outlier detection (moving median method, length of 25)
7. Crop surface to eliminate overlap in Y direction
8. Align scans
    a. Cross correlate the top skin surfaces at the boundaries, after reversing surface so bottom of image is zero
    b. Pad edges of surfaces to align with the maximum cross correlation values
9. Calculate thickness
    a. Subtract the first and second layer of skin in the imaging plane (in each column imaged)
    b. Scale from pixels to mm, remove outliers less than 0 or greater than 5 mm
10. Align volume
    a. Using the same delays as use to align the scans, fuse the collected scans into one volume
    b. Warp the volume to adjust for the speed of the probe

This processing has three distinct outputs: a volumetric ultrasound image, an extracted surface of the hand, and skin thickness data.

5.3 Validation

Before deploying these processing techniques, they must be validated. Validation was done by imaging a surface we can dissect to examine the thickness. This is done using a cut of pork belly, chosen for its flat, well attached layer of skin, and thick dermis and epidermal layer, all similarities that make it a suitable model for human skin [76].

1. Place pork belly in tank. Run sweep in 5.5 cm increments at 400 mm/min feed rate over length of pork belly, with probe positioned over one edge.
2. Save files, note orientation of pork belly
3. Measure the dermal and epidermal layer of the pork belly with calipers at 1 cm intervals along the edge the probe was positioned to overlap
4. Manually extract thickness measurements
5. Reconstruct and measure thickness with processing
6. Compare values

The ultrasound examination obtained images shown like those in Figure 5.4.

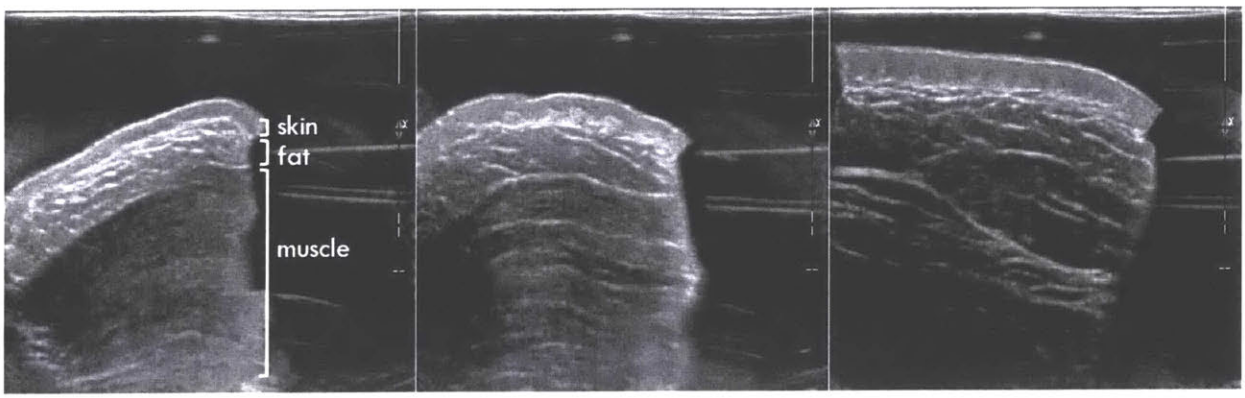

Figure 5.4: Example images of pork belly

The images above in Figure 5.4 are slices increasing in thickness along the long edge of the pork belly. The dissection examined the same layers as shown below in Figure 5.5. The dermal and epidermal layers are hard in comparison to the subcutaneous fat, easing the dissection process. The caliper measurements (Figure 5.6) are accurate approximately to the quarter millimeter. The following measurements were obtained from the sample along the long edge as shown in the surface in Figure 5.7, left to right.

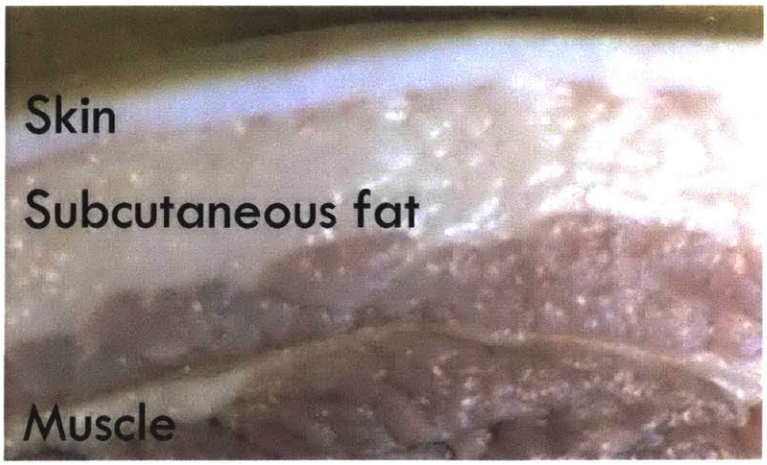

Figure 5.5: Layers in pork belly

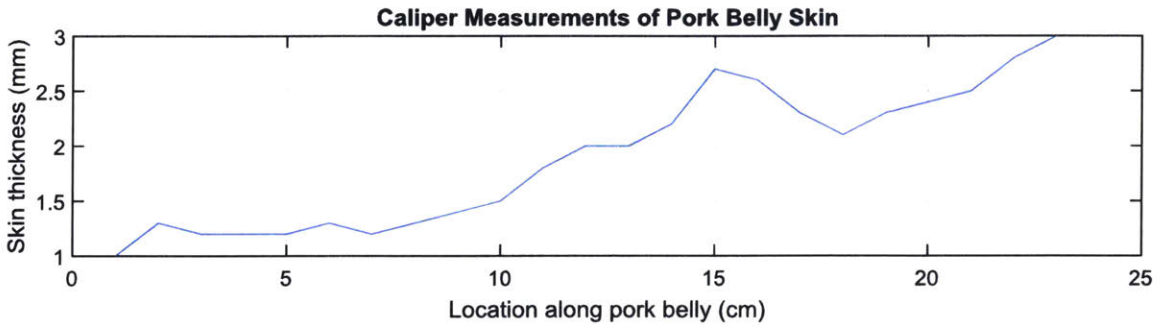

Figure 5.6: Caliper measurements of pork belly skin thickness

The resulting ultrasound volume from processing one scan is shown below in Figure 5.7, and the extracted thickness in Figure 5.8.

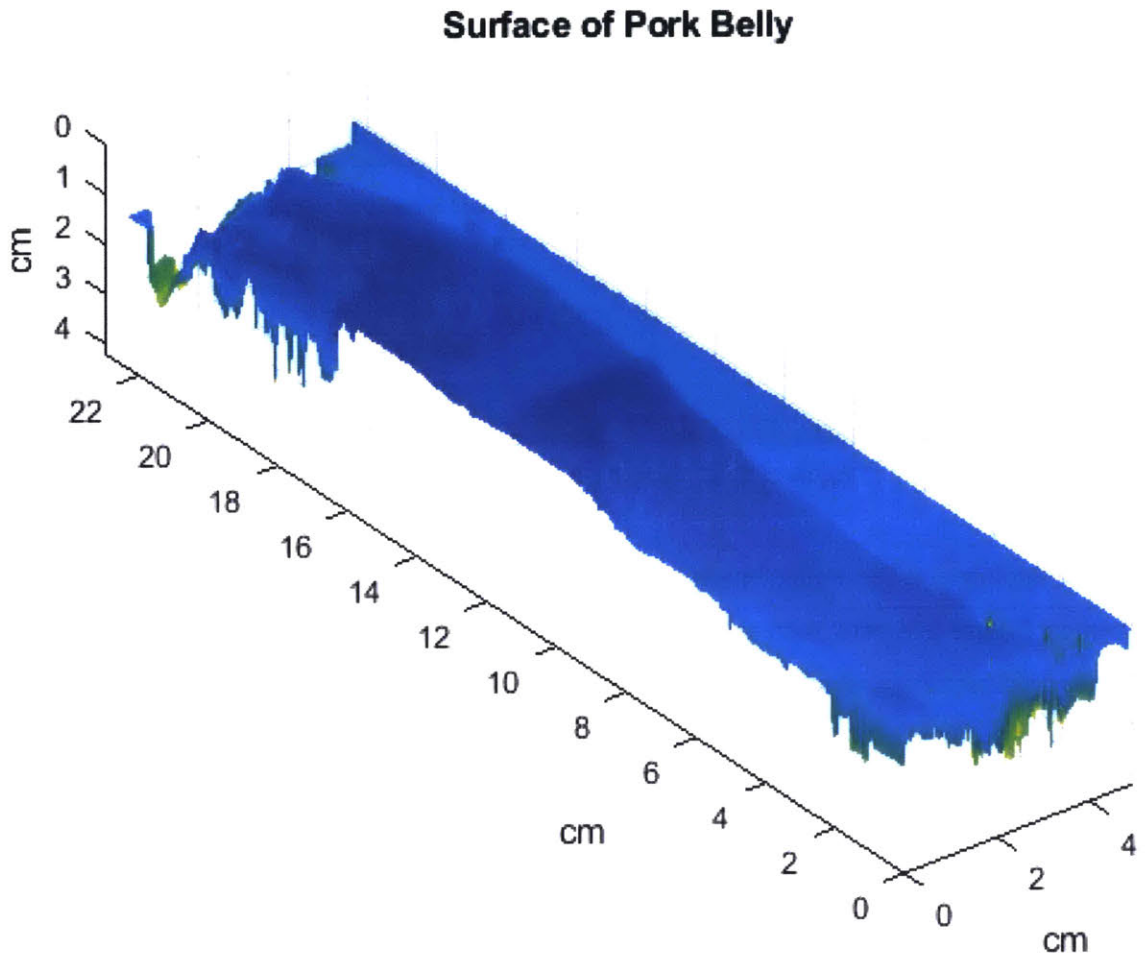

Figure 5.7: Extracted surface of pork belly

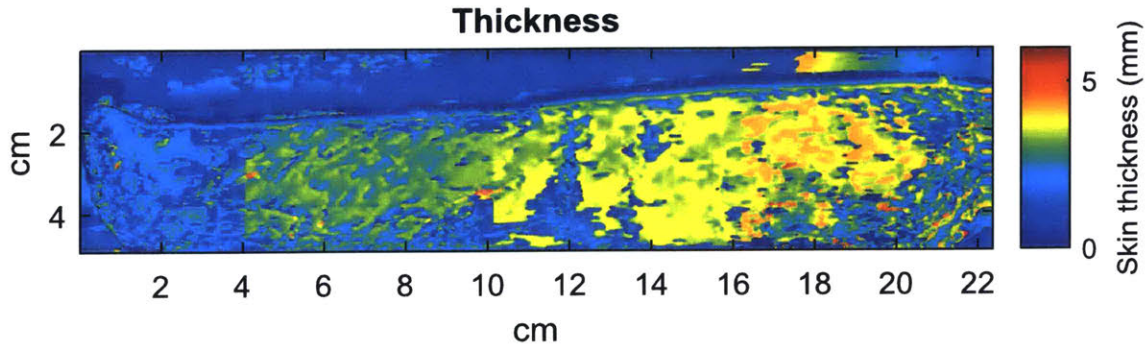

Figure 5.8: Automatically extracted vertical skin thickness of pork belly

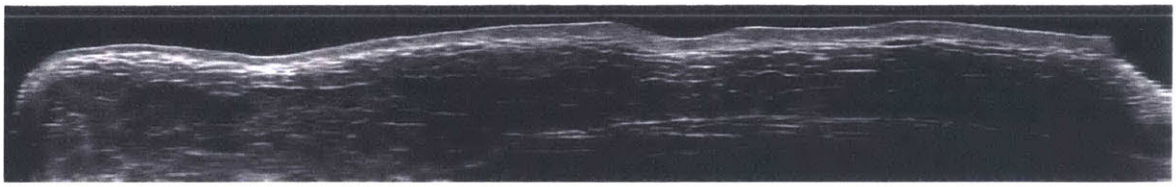

Figure 5.9: Ultrasound image along the plane measured with calipers

Figure 5.10: Automatically extracted skin boundaries

The skin thickness at the approximately sampled locations was extracted manually for the image, shown in Figure 5.9, and with the automatic processing method, shown in Figure 5.10. The processed skin thickness is averaged in 20 pixel regions, and shown with the caliper measurements in Figure 5.11.

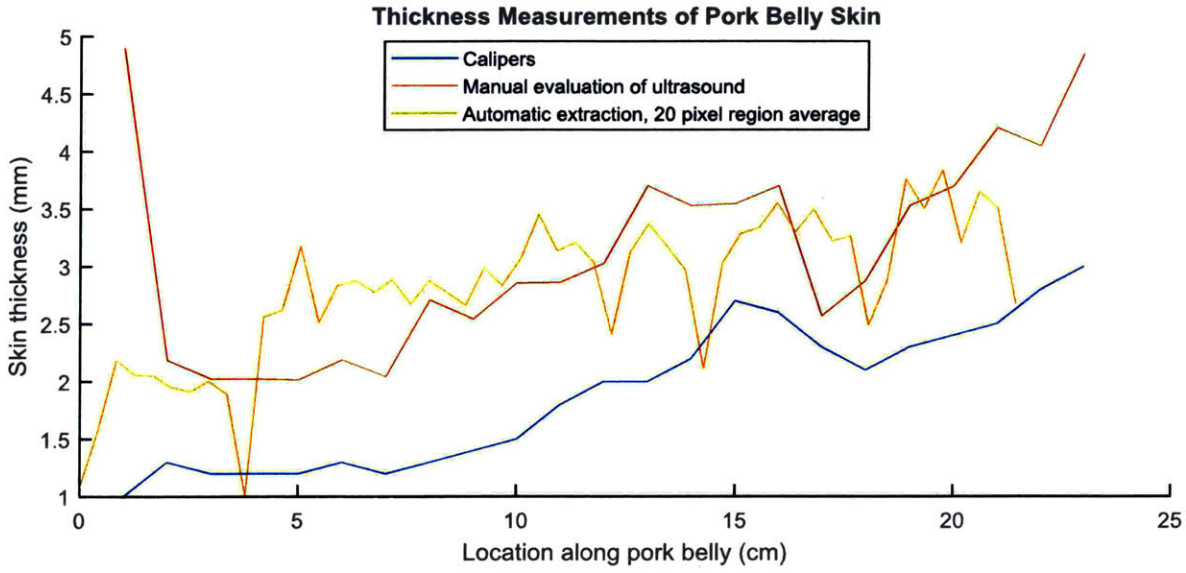

Figure 5.11: Thickness Measurement by calipers, manual evaluation, and automated extraction

For the manual extraction, there is a relatively constant offset of 1 mm from the caliper measurements. The offset may be from the thickness of the entry echo, the bright line that occurs

in ultrasound images at the boundary of the water and skin. A correction for the thickness of the entry echo could be incorporated into the skin thickness extraction with sufficient calibration. The automatic extraction clearly has significant noise due to false detections of the lower boundary, but shows a good relationship to the manual ultrasound extraction.

CHAPTER

6

RESULTS AND DISCUSSION

Human volunteers were tested at MIT in laboratory 35-017 under IRB Protocol Number 1607640016R001. 2 men and 3 women were imaged. The following will demonstrate the volume construction and skin boundary extraction, first showing the type of data generated and the visualization possible, and then testing the data by comparing the skin thickness of men and women, and repeated measurements.

6.1 Overall performance demonstration

The data is collected in 16 to 18 ultrasound videos of the arm. These are processed into 3 initial outputs, the surface of the hand (Figure 6.1), an ultrasound volume, which can be viewed in 3 imaging planes (Figure 6.2), and a thickness map (Figure 6.3). The surface allows for confirmation of successful stitching. While some are successful (Figure 6.4), others are not fully aligned with the cross correlation method (Figure 6.5), particularly when the actual delay would be larger or the arm cross section overlaps with the boundary of the probe. The jumps between images visible in the stitching can also be attributed in inconsistent speed of the stepper motors; improvements are discussed in the next chapter.

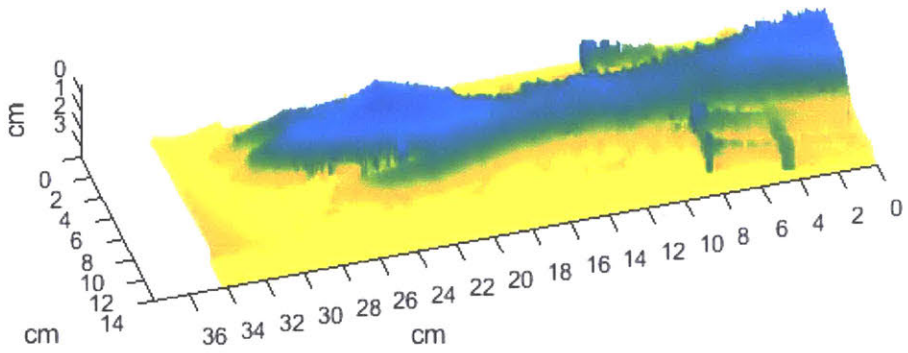

Figure 6.1: Extracted surface of hand

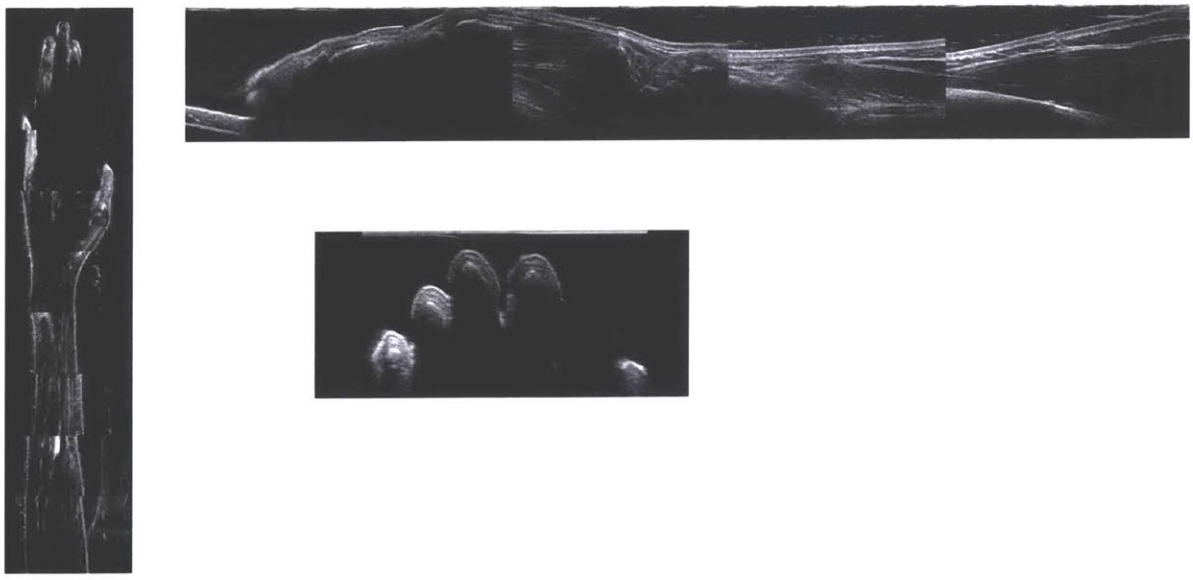

Figure 6.2: Volume viewed from top of arm (left) from side (top) and as a cross section in the fingers (bottom)

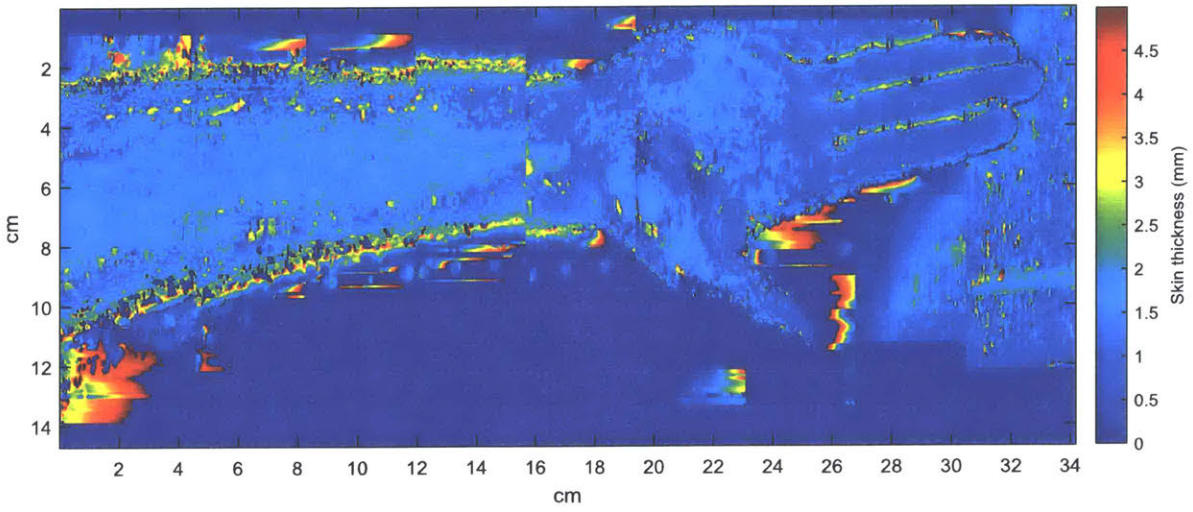

Figure 6.3: Thickness map

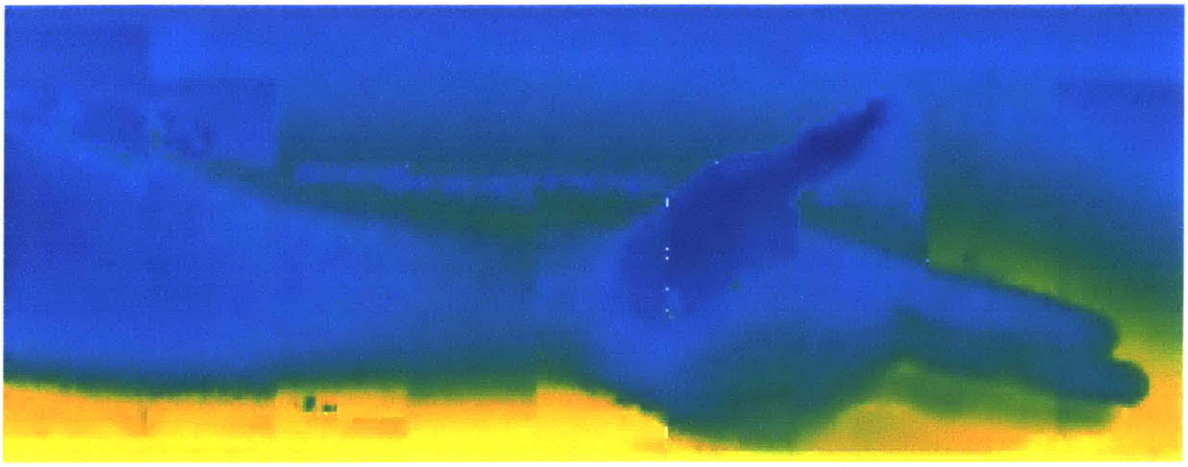

Figure 6.4: Successful ventral scan alignment with cross correlation

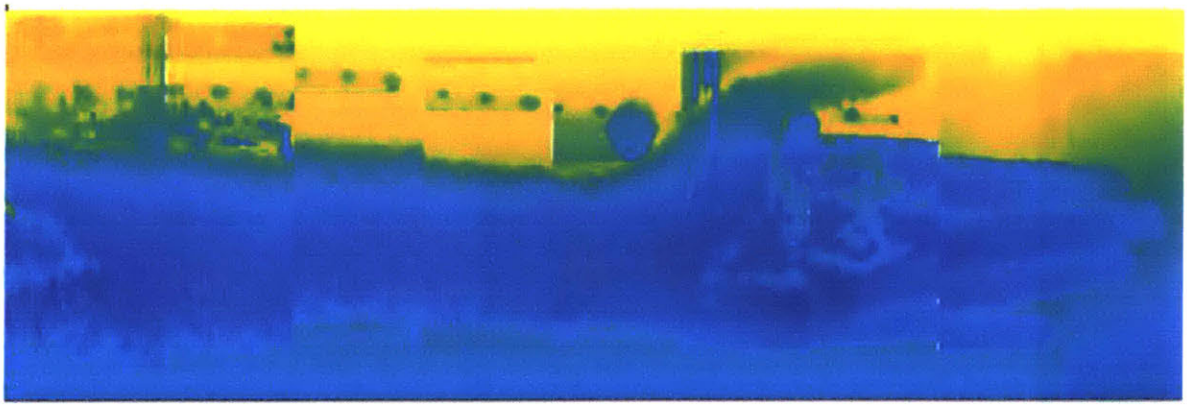

Figure 6.5: Dorsal scan with error in finger alignment from cross correlation

We can also examine the success of extracting the skin thickness on a local level. Figure 6.6 shows a successful segmentation of the skin layer. In the fingertips, this boundary is obscured at the current ultrasound frequency, shown in Figure 6.7. In the rest of the hand, debris or any element which causes a reflection or echo may lead to false detections, as shown in Figure 6.8. Figure 6.9 shows the most common failure modality: the presence of any arm hair, which reflects ultrasound waves and causes an initial spike in the gradient above the arm. While detections of the bone are minimized with the expected thickness parameter, the current method cannot overcome the presence of hair to find the true skin layer.

Each of these error modes represents ways to better tailor the analysis process to the diversity of data gathered over the length of the arm. Despite this, the resulting thickness maps provide interesting initial insights.

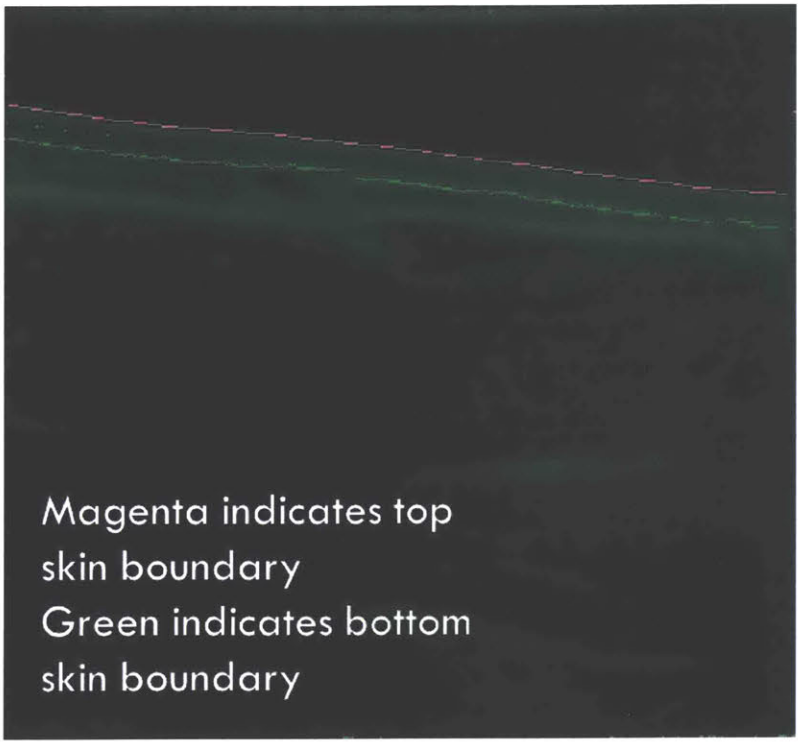

Figure 6.6: Successful skin identification in back of hand

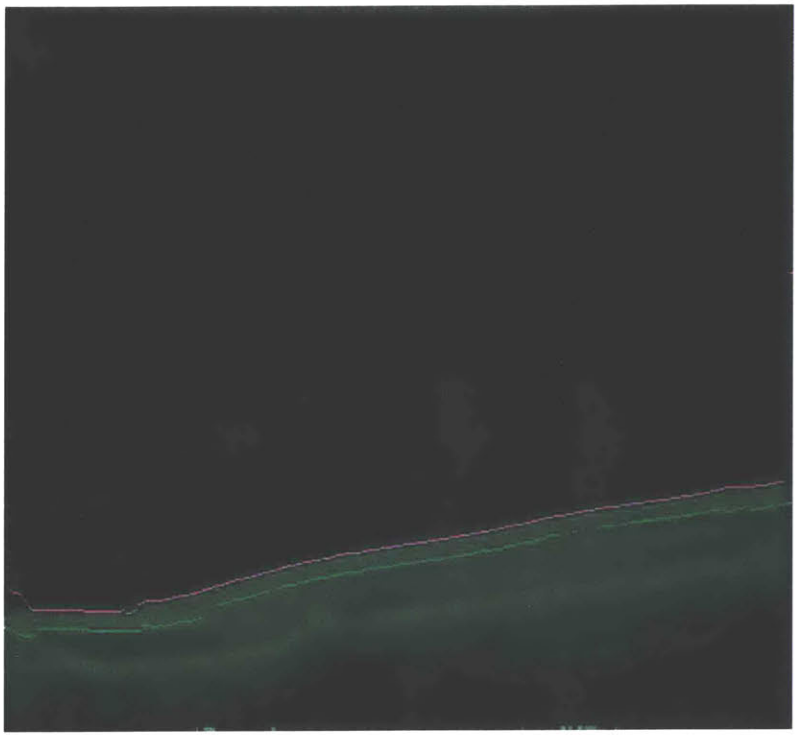

Figure 6.7: Nominally successful skin thickness in fingers due to poor imaging of boundary

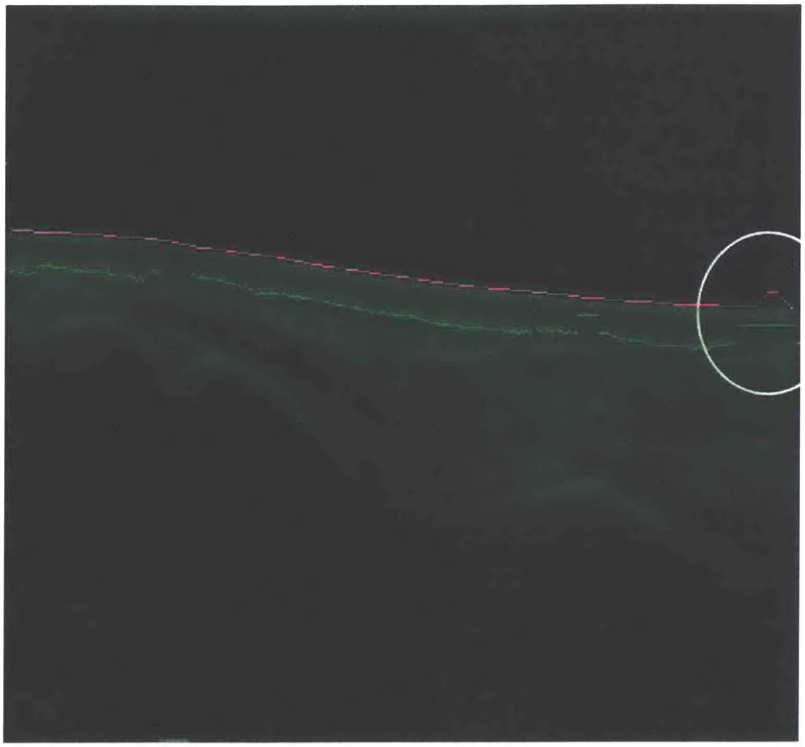

Figure 6.8: Mostly successful skin identification with errors due to debris (circled)

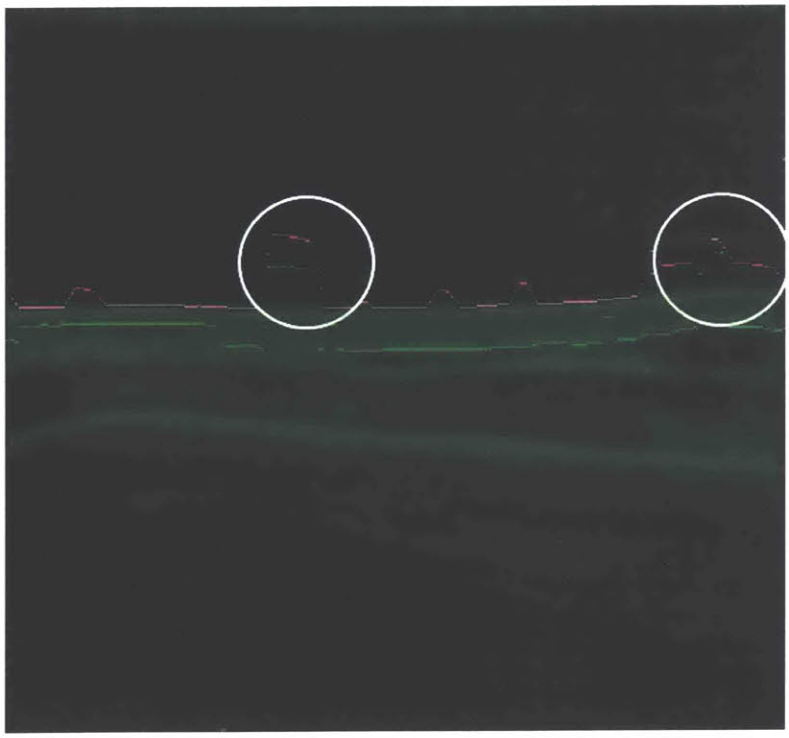

Figure 6.9: False detections due to reflections from hair (circled)

6.2 Repeated measurements

While no ground truth can be obtained for these samples, the stability of the measurements can be evaluated with two sequential scans of the same hand. Figure 6.10 and Figure 6.11 below show the surfaces extracted from two sequential scans of the ventral forearm, chosen for its lack of hair, for the best thickness results. This allows for the analysis to be tested in the absence of reflections due to hair. The hand positions are approximately the same, with the second scan showing a slightly more angled arm, and the thumb closer to the rest of the fingers.

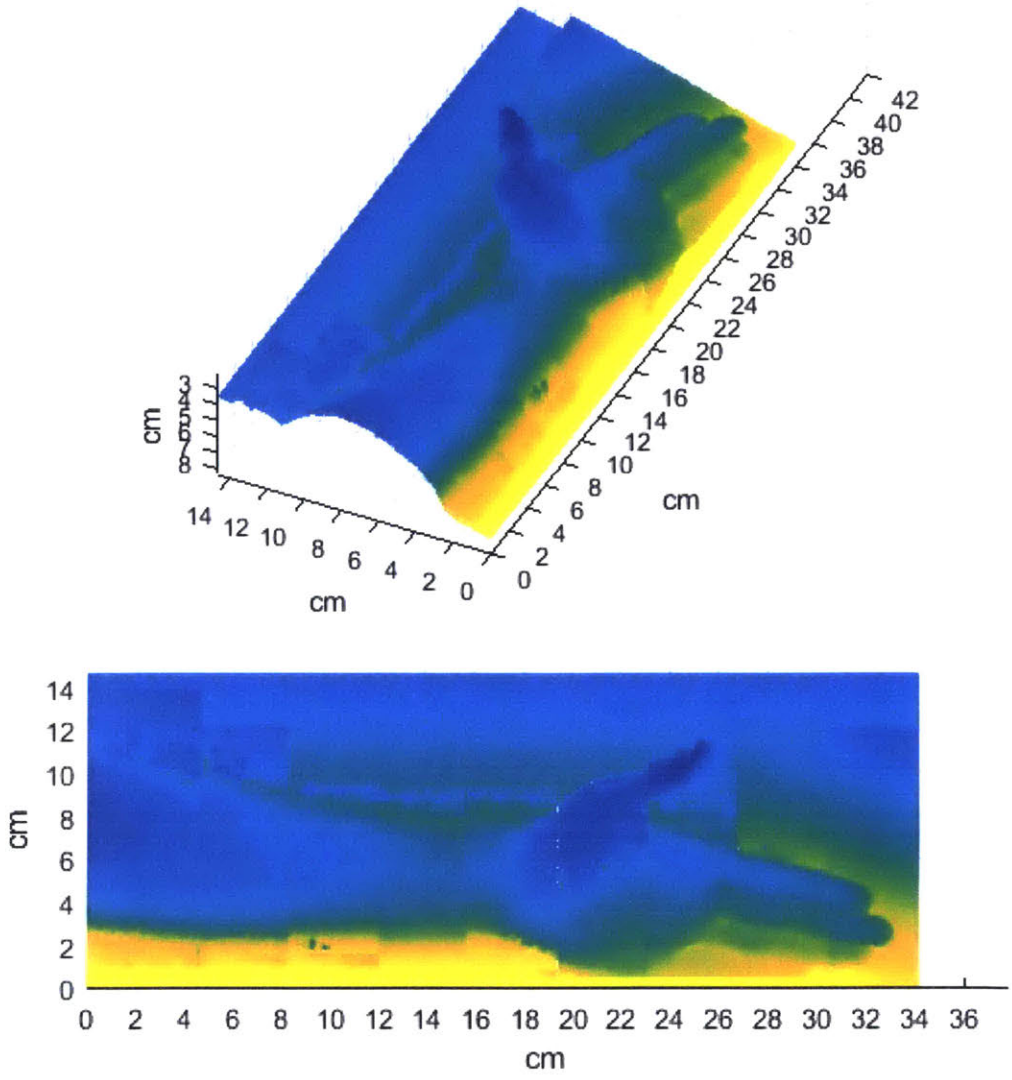

Figure 6.10: Extracted surface of first scan

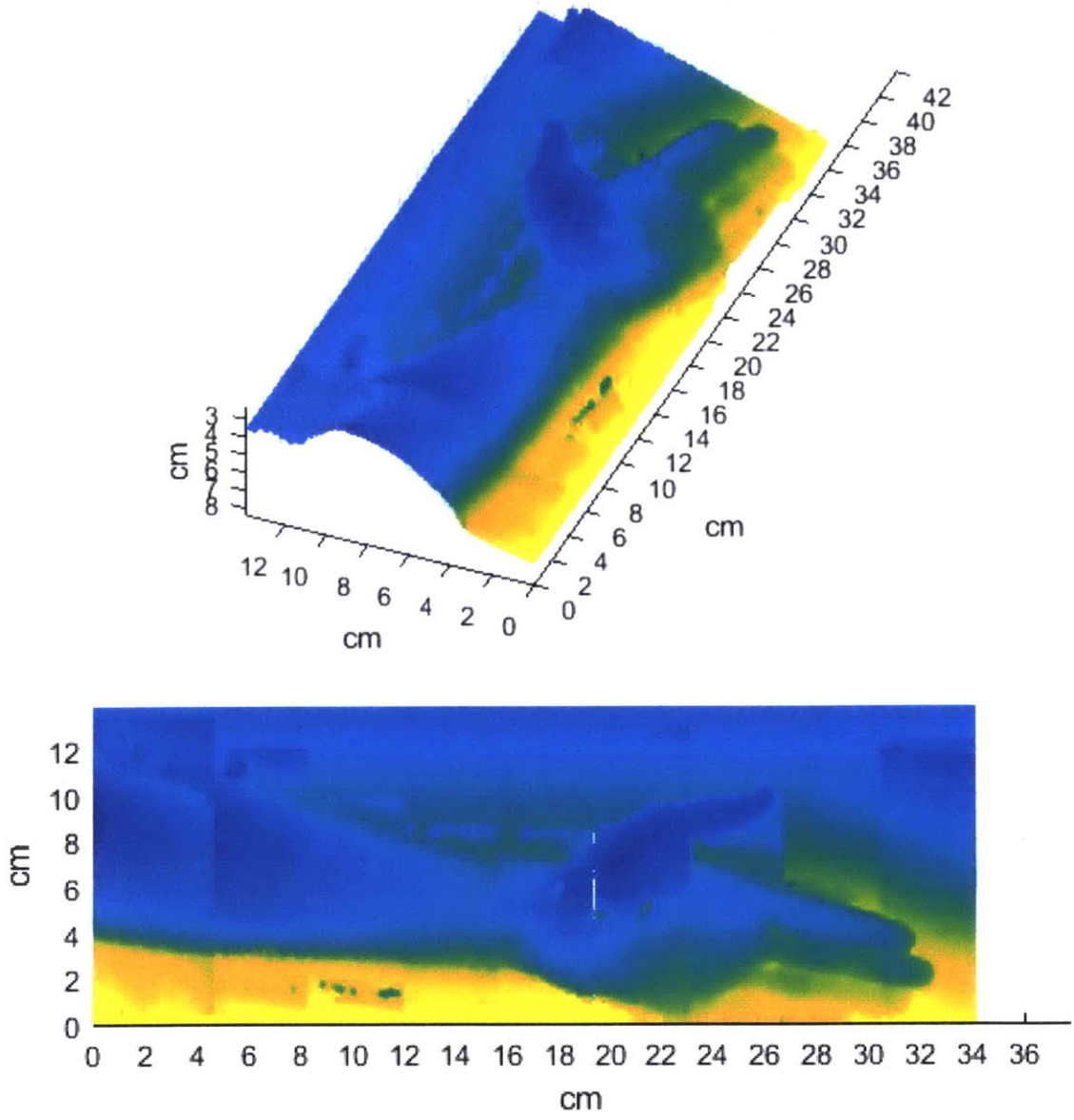

Figure 6.11: Extracted top surface of second scan

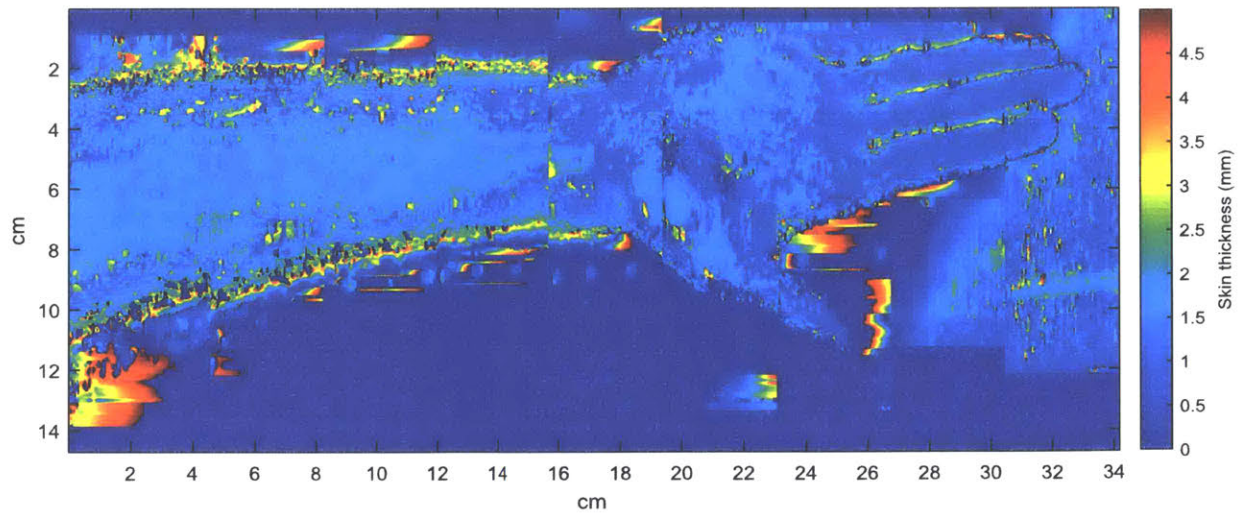

Figure 6.12: Thickness of first scan

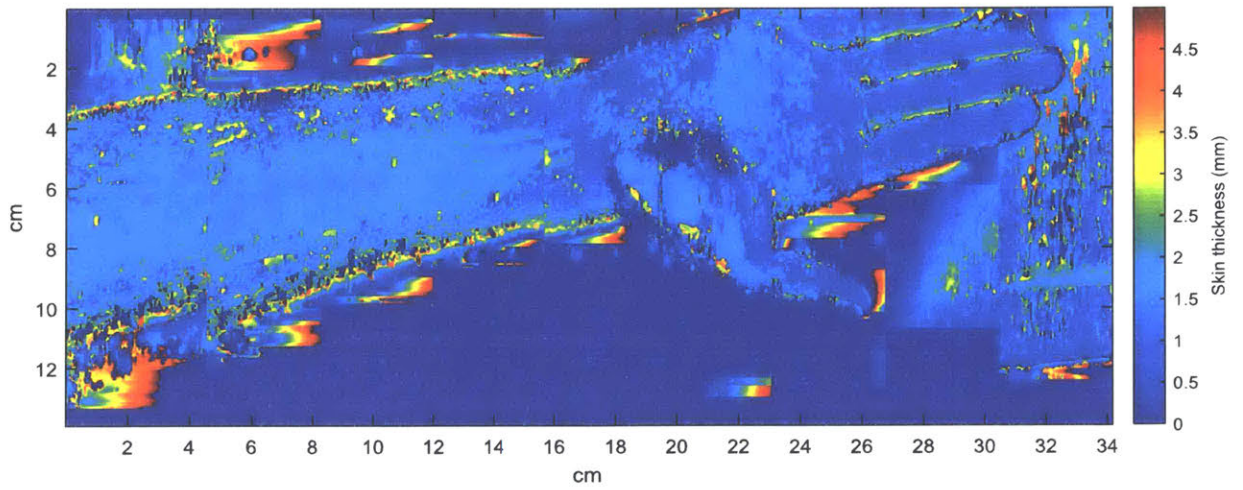

Figure 6.13: Thickness of second scan

Figure 6.12 and Figure 6.13 below show the skin thickness maps for the two sequential scans. By inspection, we can see that the thickness extracted is quite similar, thicker in the forearms, and thinner in the fingertips. While it is likely that some false detections are present, this continuity is promising for the ability to obtain similar ultrasound images to process from sequential imaging attempts. To create a more quantitative comparison, we can examine the average thickness at different locations along the arm. Figure 6.14 and Figure 6.15 show the thickness of 20 pixel square areas of the arm. This smoothing makes the visual comparison easier, and also allows for the numerical comparison, due to the approximately repeatable hand positioning. Figure 6.16 shows the residual plot of the absolute value of error in thickness. The regions of higher error are at or

outside the boundary of the arm; including these regions the average error is 0.36 mm. A sample along the centerline of the hand is shown in Figure 6.17. The signals track closely and the error between the two remains smaller than 1 mm, with the exception of the misaligned spike at 35 cm.

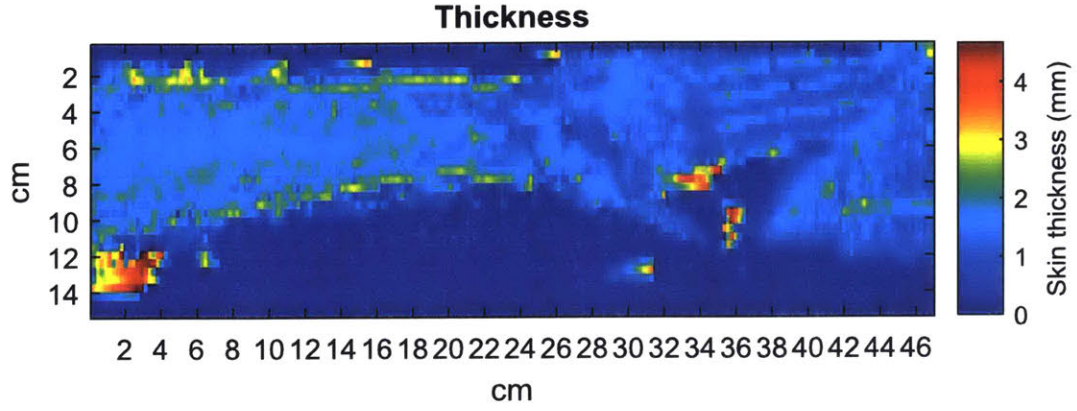

Figure 6.14: Thickness of 20 pixel square areas of first ventral arm scan

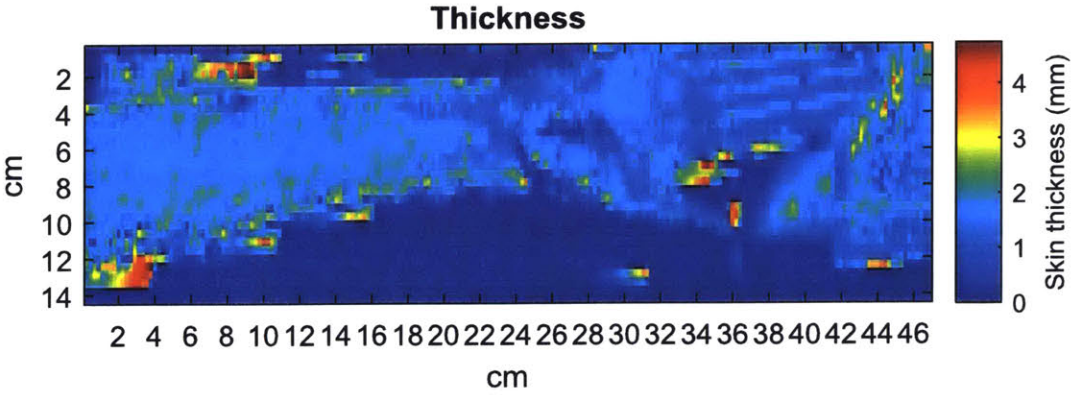

Figure 6.15: Thickness of 20 pixel square areas of second ventral arm scan

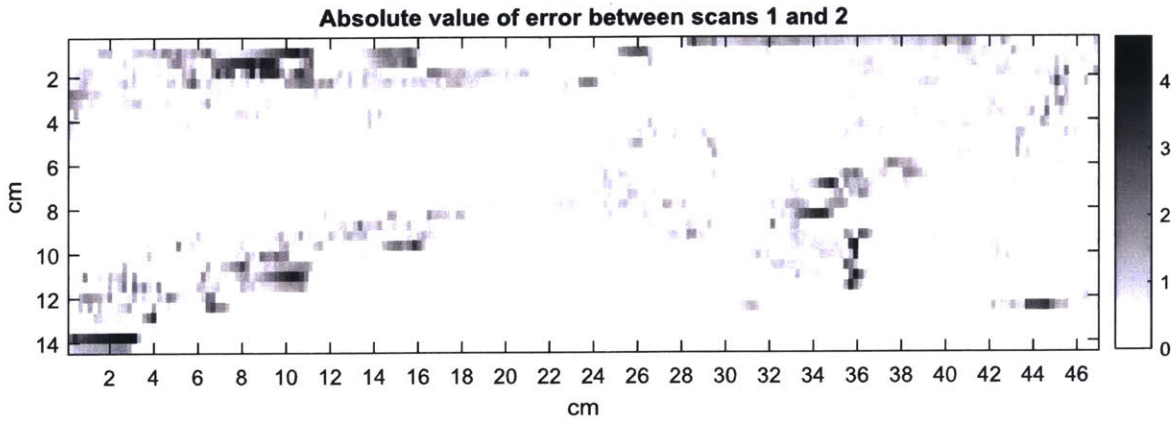

Figure 6.16: Residual plot of error between scans 1 and 2

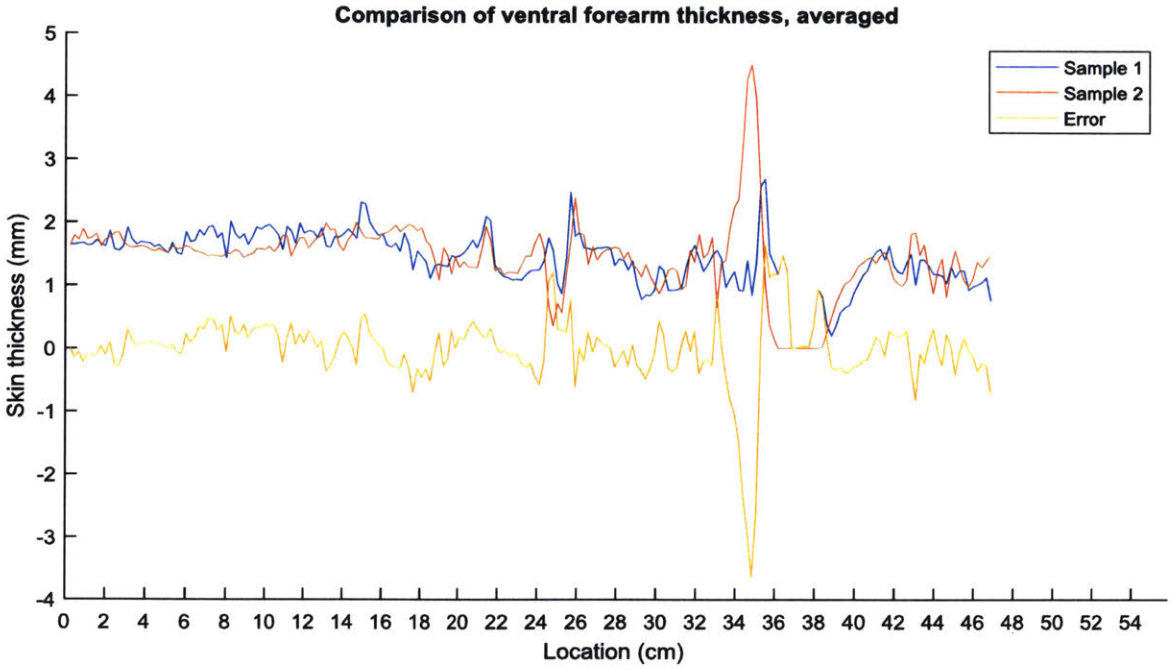

Figure 6.17: Comparison of thickness along centerline of ventral arm scans

Figure 6.17 makes it clear that the measurements have captured the same thickness data. Future studies might use the average skin thickness on the palm, the percentage of skin above a certain thickness, or more accurately map the locations on the body from one scan to another to form a thickness map that shows change from one scan to another on all documented parts of the forearm.

6.3 Gender differences

Average skin thickness is loosely correlated with gender, with men tending to have thicker skin than women. With the small sample size used in this study, no sweeping conclusions can be made, but it provides another potential reference point to evaluate the algorithm. The figures below show dorsal and ventral skin thickness for the 4 volunteers. The male volunteers had much more significant hair, which can be observed in the noisy thickness pattern to the left side of Figure 6.18 and Figure 6.19, but the presence of some hair for the women in Figure 6.20 and Figure 6.21 still causes significant disruption to the successful extraction of the thickness, making this comparison inconclusive. Aliasing in flat areas near the thumb (seen in Figure 6.18 and Figure 6.19) is due to reflections off the surface of the armrest and pegs for hand placement.

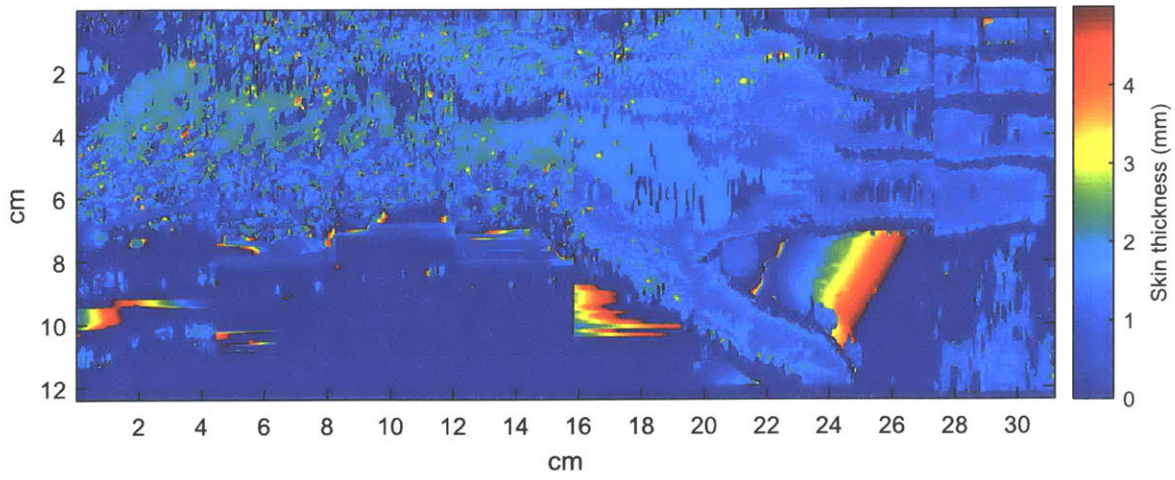

Figure 6.18: Skin thickness of 26 year old male

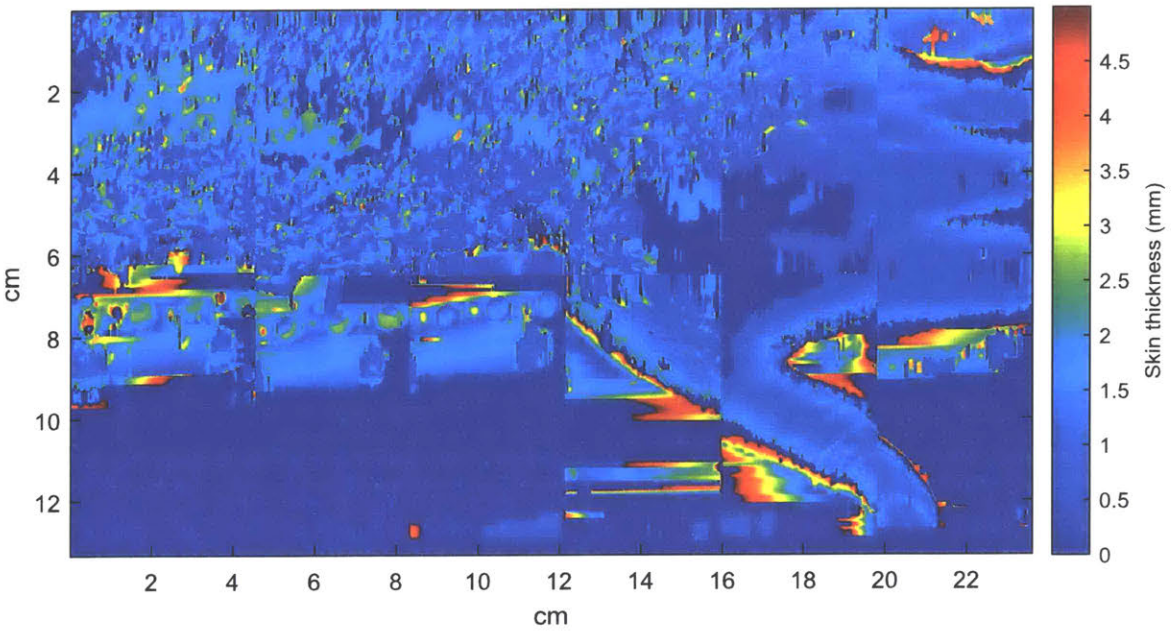

Figure 6.19: Skin thickness of 25 year old male

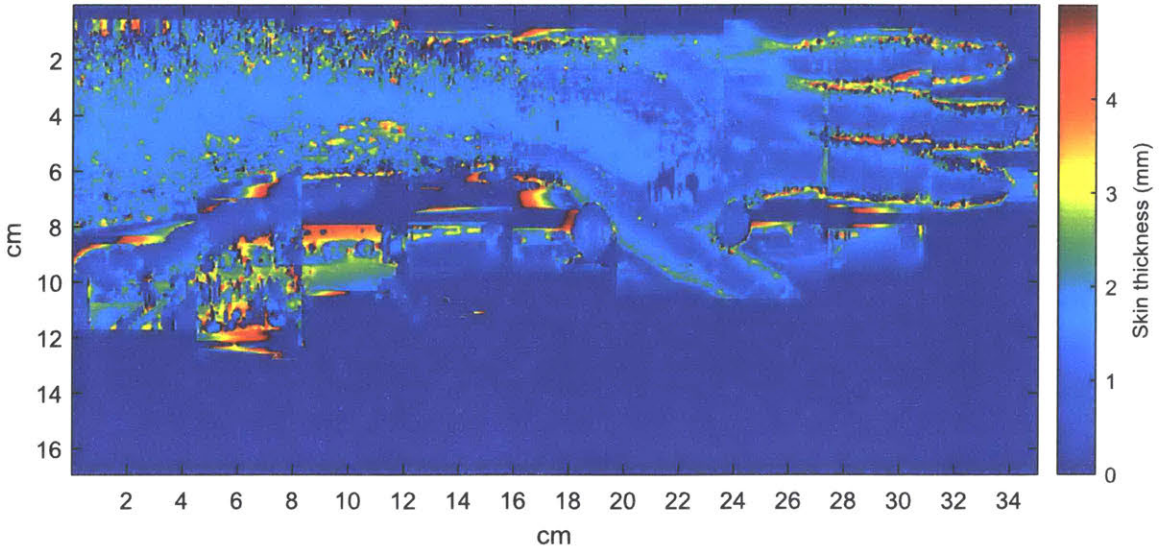

Figure 6.20: Skin thickness of 25 year old woman

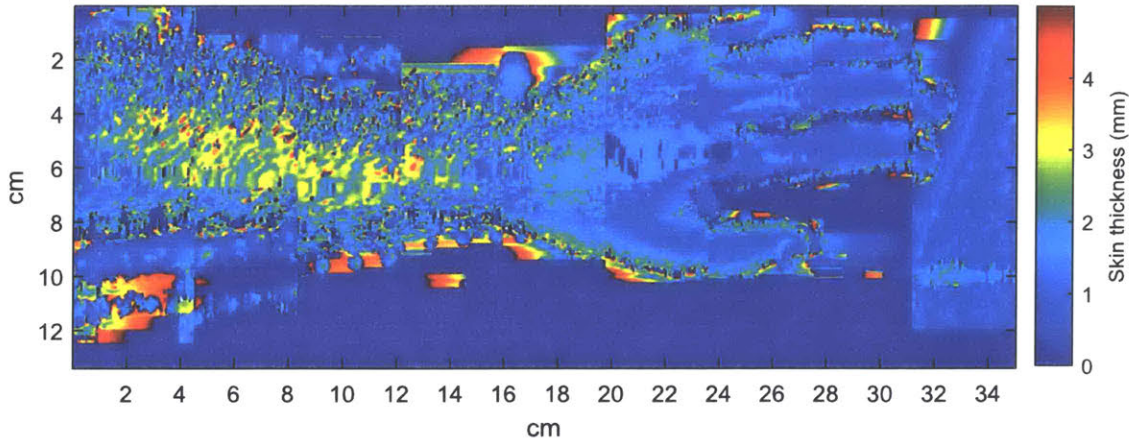

Figure 6.21: skin thickness of 26 year old woman

6.4 Imaging other structures of interest

In addition to the skin thickness measurements, the volumes constructed allow the image to be easily sliced and viewed, which brings many interesting tendons and ligaments into view. Figure 6.22 shows the extensor tendon in the middle finger of a 25 year old female.

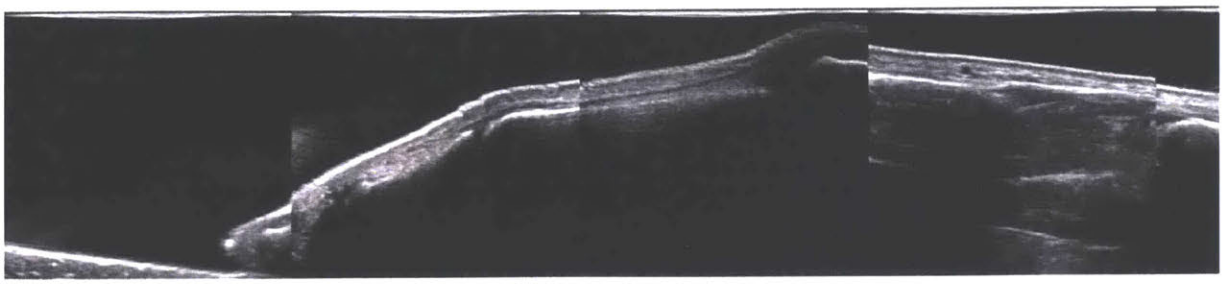

Figure 6.22: Extensor tendon in middle finger (female, 25 years old)

Figure 6.23 shows the middle figure extensor tendon in the back of the hand of a 26 year old male. This tendon is more hypoechoic (less reflective of the ultrasound, and thus darker) than the other subjects. It is possible this is due to tendon inflammation, as this subject is a rock climber and former baseball player, but also potentially due to anisotropy (in which the sound is reflected away from the transducer) due to the angle of a transducer [77][78]. Veins are also particularly prominent in this scan.

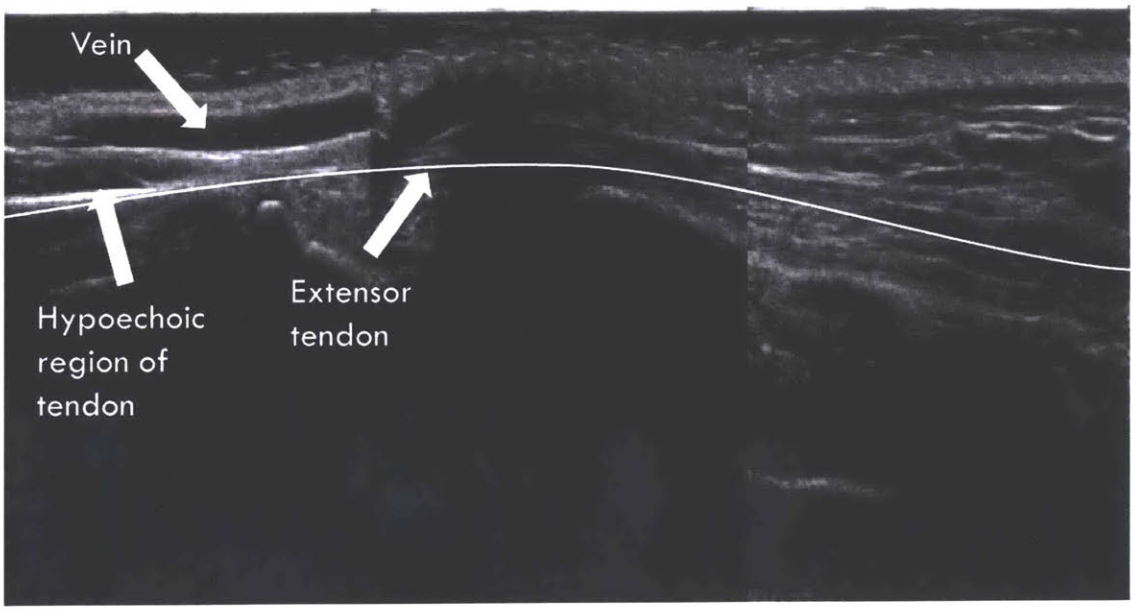

Figure 6.23: Extensor tendon on back of hand (male, 26 years old)

Outside the hand in the forearm, muscles and tendons are clearly delineated due to the increased thickness of soft tissue structures and less refraction off the deeper bones, as compared to the fingers. This is shown in Figure 6.24 and Figure 6.25, which show cross sections taken in the

direction of the probe and orthogonal to the probe respectively. Some misalignment of the reconstruction can be observed, primarily due to the speed variability of the stepper motors. When using these ultrasound volumes, it should be noted that there is a degradation in quality outside the plane of the original ultrasound, due to the frame rate and speed of translation of the probe (caused by the short maximum scanning time. Despite this, the images provide fascinating views of the huge number of soft tissue structures of the hand and arm.

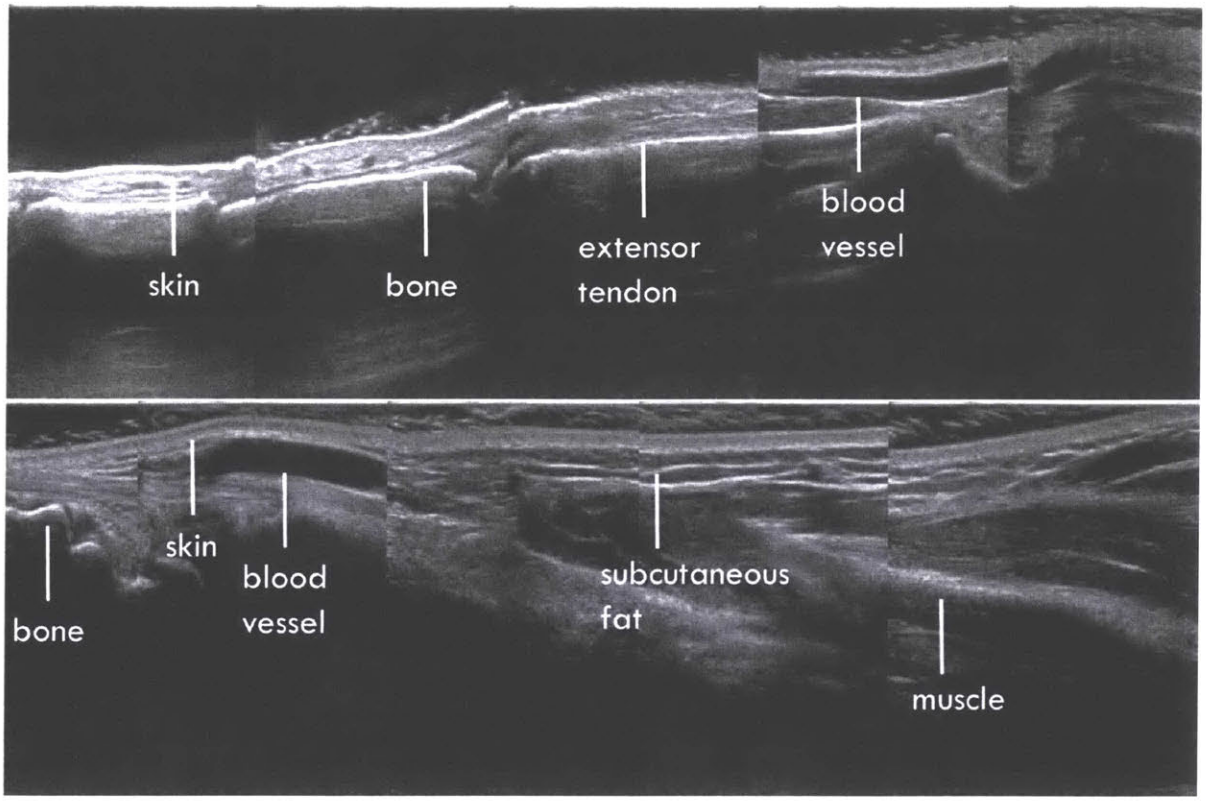

Figure 6.24: Dorsal ultrasound along fingers (top) and forearm (bottom) showing differing levels of detail

Figure 6.25: Dorsal ultrasound across fingers (left) and forearm (right) showing differing levels of detail

CHAPTER

7

CONCLUSIONS AND FUTURE WORK

7.1 Future Work

7.1.1 Imaging Improvements

Before acknowledging the improvements possible in the design and analysis, we will first delve into the limitations imposed by the ultrasound machine itself. With the ability to integrate fully with an ultrasound machine and take data natively, many problems would be removed. In the absence of full access to the ultrasound data, the first, and by far most serious, shortcoming is the ability to only take a ten second video, which requires repetitive sweeps be stitched together to cross even the 130 mm of a hand at 400 mm/min, the maximum rate at which the stepper motors operate smoothly. Second, the lack of a universal time clock and the ability to synchronize the ultrasound data with the position of the probe introduces another layer of error. While the cross correlation procedure provides acceptable results, it introduces unnecessary error and sometimes fails if one probe sweep contains erroneous surface detections. Removing this source of error would streamline the volume reconstruction, and make it successful independent of the surface extraction. A probe able to take extended videos could also allow for alternative procedures to synchronize the time clocks. The third limiting factor is the frequency of the ultrasound probe, 12 MHz. While this frequency allows for a greater depth of penetration and a more complete ultrasound reconstruction of the arm and hand, it is insufficient for reliable skin measurements, particularly in the fingertips, where thin skin, underlying hypoechoic connective tissue, and the refraction from the bone close to the surface obscure the skin layer. The area of skin thickness extraction could be improved by increasing the frequency of the probe. This may necessitate smaller sampling areas, access to channel data, or dynamic focusing, because of the small field of view for extremely high frequency probes.

7.1.2 RSTM Device Improvements

The design of the RSTM Device for probe constraint and translation has a number of areas of improvement, particularly the probe motion, patient experience, and mechanism refinement. All three of these contribute to imaging quality, positioning precision and accuracy, and the subsequent precision and accuracy of the volume reconstructions and skin thickness measurements.

First, the probe motion can be improved in a number of ways. Most importantly, the speed could be made more consistent, or recorded more accurately. In a bigger tank with room to ramp up the speed, the sampling frequency would be more constant, and the position on the X axis more repeatable and accurate. Alternately, including encoders with the stepper motors, if properly synced to the ultrasound measurements, would remove most of the error in the X motion, which effects volumetric reconstructions and skin thickness measurement. Additionally, the motion could be automated in 3 axes. While not necessary, 3-axis would ease the burden on the operator, while also eliminating any errors due to operator variability in placing the kinematic coupling. With an ultrasound machine able to take extended videos and a fully automated machine in 3 axes, the full scan would take approximately 30 seconds for each of 9 to 10 sweeps in the X direction, for a total of 4.5 to 5.0 minutes. Another potential improvement to the probe motion would be to customize curved probe motion to each subject's arm contours. This would allow for better focus on the skin surface for extracting the second boundary.

Ergonomics and patient experience, as in most first prototypes, are significant areas of potential improvement. The rotating armrest mechanism, while useful and quick to change from side to side, creates instabilities if the patient wants to angle their elbow on the higher side of the armrest. The ability to lock it securely into place would help with this problem. An adjustable tank height, or an adjustable chair or stool, and an adjustable armrest height would help the standing test be more comfortable, tailored to patients elbow height and upper arm length. Increased patient comfort will increase the reliability of volume reconstruction. A larger tank would increase the comfort of larger patients, as the current setup does not account adequately for the space required for a wider upper arm.

Finally, there is the potential to improve and innovate in a number of the mechanisms of the machine. The stiffness of the mounts for the kinematic coupling contribute significantly to the error. This can be addressed with the 3 axis automation, or by increasing the stiffness of the frame with another material or potentially further cross bracing. The motor accuracy could be improved

with the addition of encoders, as well as a more reliable, better maintained leadscrew system. The coupling to attach the probe is largely very successful, but could be further refined with a standardized plastic locking mechanism through the same molding procedure or a 3D scanning procedure.

The design of the RSTM Device has a number of areas of improvement, particularly the probe motion, patient experience, and mechanism refinement. All three of these contribute to imaging quality, positioning precision and accuracy, and the subsequent precision and accuracy of the volume reconstructions and skin thickness measurements. The most crucial improvements are making the accuracy of the motor positions more constant, by regulating speed or measuring the position, and syncing it to the time of the ultrasound probe videos.

7.1.3 Analysis Improvements

The analysis procedure is the one of the main areas for potential improvements of the current prototype. The primary issue with extracting the top surface of the skin is the presence of hair. These false detections could be countered in future iterations by eroding the image with a disk greater than the thickness of the hair, or an alternate line detection method which takes into account continuity. Improvements will have to balance results and computational intensity. The bottom surface of the dermis is extracted with significant amounts of noise and false detections. By using the surrounding extractions to inform the location of the probable boundary, or seeding the boundary manually in each image, the surface extracted could be more smoothly extracted. The skin thickness can correspond more directly to the actual skin thickness with the introduction of a method to measure the tangent plane to a particular location on the skin, and measure the thickness perpendicular to that. Without smoother extracted skin surfaces both top and bottom, measuring this way introduces too much extra error, which is why it was not included in this iteration.

Finally, there is also room for speeding up the analysis, potentially to allow results to be immediately available following a scan. Faster reconstructions would allow for the clinician to retest in the case of inadequate input. Methods to do this likely include moving the code from a MATLAB prototype into a production code language that allows for more efficient memory use when processing large datasets.

7.2 Conclusions

The RSTM Device and analysis procedures present a proof of concept for the volumetric ultrasound and automatic skin thickness extraction over the surface of the arm. While the automation of skin thickness extraction has room for substantial improvement, this is the first attempt to extend skin thickness measurement beyond a single 2D image. The constructed volume can be used in a wide variety of applications, and viewed along an imaging plane in the same manner of volumetric imaging techniques, like CT and MRI. This has the potential to make ultrasound diagnostic imaging more applicable for soft tissue injuries in the hand and arm. The extension of skin thickness measurement to a larger area eliminates error from different probe positioning. As the extraction of the skin boundaries improves, the dramatic increase in sampling will create more robust metric to allow for close tracking of the progression of scleroderma to evaluate individual treatment plans and the efficacy of experimental treatments.

REFERENCES

[1] D. L. Sackett, W. M. Rosenberg, J. A. Gray, R. B. Haynes, and W. S. Richardson, "Evidence based medicine: what it is and what it isn't.," *BMJ*, vol. 312, no. 7023, pp. 71–2, Jan. 1996.

[2] and M. V. Stephan El Gammal , Claudia El Gammal , Peter Altmeyer, "Sonography of the Skin," in *Non Invasive Diagnostic Techniques in Clinical Dermatology*, 2014, p. pp 135-156.

[3] V. D. Steen and T. A. Medsger, "Changes in causes of death in systemic sclerosis, 1972-2002.," *Ann. Rheum. Dis.*, vol. 66, no. 7, pp. 940–4, Jul. 2007.

[4] M. Gilbertson, B. Anthony, and S.-Y. Sun, "Handheld Force Controlled Ultrasound Probe," *J. Med. Device.*, vol. 4, no. 2, p. 027540, Jun. 2010.

[5] M. W. Gilbertson and B. W. Anthony, "An ergonomic, instrumented ultrasound probe for 6-axis force/torque measurement," in *2013 35th Annual International Conference of the IEEE Engineering in Medicine and Biology Society (EMBC)*, 2013, vol. 2013, pp. 140–143.

[6] B. J. Ranger *et al.*, "3D optical imagery for motion compensation in a limb ultrasound system," 2016, vol. 9790, p. 97900R.

[7] S.-Y. Sun, M. Gilbertson, and B. W. Anthony, "Probe localization for freehand 3D ultrasound by tracking skin features.," *Med. Image Comput. Comput. Assist. Interv.*, vol. 17, no. Pt 2, pp. 365–72, 2014.

[8] O. Distler and A. Cozzio, "Systemic sclerosis and localized scleroderma—current concepts and novel targets for therapy," *Semin. Immunopathol.*, vol. 38, no. 1, pp. 87–95, Jan. 2016.

[9] S. A. Jimenez, E. Hitraya, and J. Varga, "PATHOGENESIS OF SCLERODERMA: Collagen," *Rheum. Dis. Clin. North Am.*, vol. 22, no. 4, pp. 647–674, Nov. 1996.

[10] S. E. Bendeck and H. T. Jacobe, "Ultrasound as an outcome measure to assess disease activity in disorders of skin thickening: An example of the use of radiologic techniques to assess skin disease," *Dermatol. Ther.*, vol. 20, no. 2, pp. 86–92, Mar. 2007.

[11] T. Arkachaisri and S. Pino, "Localized scleroderma severity index and global assessments: a pilot study of outcome instruments.," *J. Rheumatol.*, vol. 35, no. 4, pp. 650–7, Apr. 2008.

[12] G. P. Rodnan, E. Lipinski, and J. Luksick, "SKIN THICKNESS AND COLLAGEN CONTENT IN PROGRESSIVE SYSTEMIC SCLEROSIS AND LOCALIZED SCLERODERMA."

[13] D. E. Furst *et al.*, "The modified Rodnan skin score is an accurate reflection of skin biopsy thickness in systemic sclerosis.," *J. Rheumatol.*, vol. 25, no. 1, pp. 84–8, Jan. 1998.

[14] M. J. J. Kerns, M. A. Darst, T. G. Olsen, M. Fenster, P. Hall, and S. Grevey, "Shrinkage of cutaneous specimens: formalin or other factors involved?," *J. Cutan. Pathol.*, vol. 35, no. 12, pp. 1093–1096, Dec. 2008.

[15] K. W. Moon, R. Song, J. H. Kim, E. Y. Lee, E. B. Lee, and Y. W. Song, "The correlation between durometer score and modified Rodnan skin score in systemic sclerosis," *Rheumatol. Int.*, vol. 32, no. 8, pp. 2465–2470, Aug. 2012.

[16] G. E. Piérard, T. Hermanns-Lê, and C. Piérard-Franchimont, "Scleroderma: skin stiffness assessment using the stress–strain relationship under progressive suction," *Expert Opin. Med. Diagn.*, vol. 7, no. 2, pp. 119–125, Mar. 2013.

[17] S. Y. Lee, A. R. Cardones, K. Nightingale, and M. Palmeri, "Characterizing sclerotic skin

stiffness with Acoustic Radiation Force Impulse (ARFI) and Shear Wave Elasticity Imaging (SWEI)," in *2015 IEEE International Ultrasonics Symposium (IUS)*, 2015, pp. 1–4.

[18] D. Rallan and C. C. Harland, "Skin imaging: is it clinically useful?," *Clin. Exp. Dermatol.*, vol. 29, no. 5, pp. 453–459, Sep. 2004.

[19] R. Kleinerman, T. B. Whang, R. L. Bard, and E. S. Marmur, "Ultrasound in dermatology: Principles and applications," *J. Am. Acad. Dermatol.*, vol. 67, no. 3, pp. 478–487, 2012.

[20] D. Vidal *et al.*, "Use of high frequency ultrasonography in dermatology departments in Spain," *Dermatol. Online J.*, vol. 22, no. 2, Jan. 2016.

[21] G. B. Jemec, M. Gniadecka, and J. Ulrich, "Ultrasound in dermatology. Part I. High frequency ultrasound.," *Eur. J. Dermatol.*, vol. 10, no. 6, pp. 492–7, Aug. 2000.

[22] J. K. Patel, S. Konda, O. A. Perez, S. Amini, G. Elgart, and B. Berman, "Newer technologies/techniques and tools in the diagnosis of melanoma.," *Eur. J. Dermatol.*, vol. 18, no. 6, pp. 617–31.

[23] R. Vilana *et al.*, "Preoperative Assessment of Cutaneous Melanoma Thickness Using 10-MHz Sonography," *Am. J. Roentgenol.*, vol. 193, no. 3, pp. 639–643, Sep. 2009.

[24] N. Meyer *et al.*, "High-frequency ultrasonography but not 930-nm optical coherence tomography reliably evaluates melanoma thickness *in vivo* : a prospective validation study," *Br. J. Dermatol.*, vol. 171, no. 4, pp. 799–805, Oct. 2014.

[25] C. L. Evans, "Peering under the skin: measuring melanoma depth with ultrasound and optical coherence tomography," *Br. J. Dermatol.*, vol. 171, no. 4, pp. 690–691, Oct. 2014.

[26] A. Varkentin *et al.*, "Comparative study of presurgical skin infiltration depth measurements of melanocytic lesions with OCT and high frequency ultrasound," *J. Biophotonics*, vol. 10, no. 6–7, pp. 854–861, Jun. 2017.

[27] M. Coßmann and J. Welzel, "Evaluation of the atrophogenic potential of different glucocorticoids using optical coherence tomography, 20-MHz ultrasound and profilometry; a double-blind, placebo-controlled trial," *Br. J. Dermatol.*, vol. 155, no. 4, pp. 700–706, Oct. 2006.

[28] N. Cowan, Z. A. Coffman, R. K. Omer, C. Carter, and T. E. Doyle, "Sensitivity study of high-frequency ultrasound to skin cancer using micro-tumor mimicking phantoms," *J. Acoust. Soc. Am.*, vol. 140, no. 4, pp. 3374–3374, Oct. 2016.

[29] C. M. Botar-Jid *et al.*, "Assessment of Cutaneous Melanoma by Use of Very- High-Frequency Ultrasound and Real-Time Elastography," *Am. J. Roentgenol.*, vol. 206, no. 4, pp. 699–704, Apr. 2016.

[30] M. Schmid-Wendtner *et al.*, "Preoperative Characterization of Basal Cell Carcinoma Comparing Tumour Thickness Measurement by Optical Coherence Tomography, 20-MHz Ultrasound and Histopathology," *Acta Derm. Venereol.*, vol. 92, no. 2, pp. 132–137, Mar. 2012.

[31] M. Mogensen, B. M. Nürnberg, J. L. Forman, J. B. Thomsen, L. Thrane, and G. B. E. Jemec, "*In vivo* thickness measurement of basal cell carcinoma and actinic keratosis with optical coherence tomography and 20-MHz ultrasound," *Br. J. Dermatol.*, vol. 160, no. 5, pp. 1026–1033, May 2009.

[32] D. Raffin *et al.*, "High-frequency ultrasound imaging for cutaneous neurofibroma in patients with neurofibromatosis type I," *doi.org*, vol. 27, no. 3, pp. 260–265.

[33] M. Simons, E. G. Kee, R. Kimble, and Z. Tyack, "Ultrasound is a reproducible and valid tool for measuring scar height in children with burn scars: A cross-sectional study of the psychometric properties and utility of the ultrasound and 3D camera," *Burns*, vol. 43, no. 5, pp. 993–1001, Aug. 2017.

[34] N. A. Agabalyan, S. Su, S. Sinha, and V. Gabriel, "Comparison between high-frequency ultrasonography and histological assessment reveals weak correlation for measurements of scar tissue thickness," *Burns*, vol. 43, no. 3, pp. 531–538, May 2017.

[35] J. S. Mertens, M. M. B. Seyger, R. M. Thurlings, T. R. D. J. Radstake, and E. M. G. J. de Jong, "Morphea and Eosinophilic Fasciitis: An Update," *Am. J. Clin. Dermatol.*, vol. 18, no. 4, pp. 491–512, Aug. 2017.

[36] F. Porta *et al.*, "High frequency ultrasound can detect improvement of lesions in juvenile localized scleroderma.," *Mod. Rheumatol.*, vol. 24, no. 5, pp. 869–873, Sep. 2014.

[37] A. Sulli *et al.*, "Subclinical dermal involvement is detectable by high frequency ultrasound even in patients with limited cutaneous systemic sclerosis," *Arthritis Res. Ther.*, vol. 19, no. 1, p. 61, Mar. 2017.

[38] K. A. Nezafati *et al.*, "14-MHz Ultrasonography as an Outcome Measure in Morphea (Localized Scleroderma)," *Arch. Dermatol.*, vol. 147, no. 9, p. 1112, Sep. 2011.

[39] F. Lacarrubba, G. Pellacani, S. Gurgone, A. E. Verzì, and G. Micali, "Advances in non-invasive techniques as aids to the diagnosis and monitoring of therapeutic response in plaque psoriasis: a review," *Int. J. Dermatol.*, vol. 54, no. 6, pp. 626–634, Jun. 2015.

[40] M. Cucoş[1] *et al.*, "Conventional ultrasonography and sonoelastography in the assessment of plaque psoriasis under topical corticosteroid treatment – work in progress," *Med Ultrason*, vol. 16, no. 2, pp. 107–113, 2014.

[41] M. E. Marina, C. B. Jid, I. I. Roman, C. M. Mihu, and A. D. Tătaru, "Ultrasonography in psoriatic disease," *Rev. Med Ultrason Med Ultrason*, vol. 17, no. 3, pp. 377–382, 2015.

[42] M. Gutierrez, E. Filippucci, F. Salaffi, L. Di Geso, and W. Grassi, "Differential diagnosis between rheumatoid arthritis and psoriatic arthritis: the value of ultrasound findings at metacarpophalangeal joints level," *Eur. Radiol.*, vol. 7, no. 3, pp. 344–51, Jun. 2011.

[43] L. de V. N. Caetano, J. L. M. Soares, E. Bagatin, and H. A. Miot, "Reliable assessment of forearm photoageing by high-frequency ultrasound: a cross-sectional study," *Int. J. Cosmet. Sci.*, vol. 38, no. 2, pp. 170–177, Apr. 2016.

[44] M. Dyson, S. Moodley, L. Verjee, W. Verling, J. Weinman, and P. Wilson, "Wound healing assessment using 20 MHz ultrasound and photography," *Ski. Res. Technol.*, vol. 9, no. 2, pp. 116–121, May 2003.

[45] H. Mohafez *et al.*, "Quantitative assessment of wound healing using high-frequency ultrasound image analysis," *Ski. Res. Technol.*, May 2017.

[46] T. Sugawara, N. Nakagawa, N. Shimizu, Y. Saijo, and S. Sakai, "Facial sebaceous gland size determined by three-dimensional ultrasound tomography correlates with skin elasticity," *J. Dermatol. Sci.*, vol. 69, no. 2, pp. e50–e51, Feb. 2013.

[47] X. Wortsman and G. Jemec, "A 3D Ultrasound Study of Sinus Tract Formation in Hidradenitis Suppurativa," *Dermatol. Online J.*, vol. 19, no. 6, Jan. 2013.

[48] K. Zarchi, N. Yazdanyar, S. Yazdanyar, X. Wortsman, and G. B. E. Jemec, "Pain and inflammation in hidradenitis suppurativa correspond to morphological changes identified

by high-frequency ultrasound," *J. Eur. Acad. Dermatology Venereol.*, vol. 29, no. 3, pp. 527–532, Mar. 2015.

[49] F. Giovagnorio, C. Andreoli, and M. L. De Cicco, "Color Doppler sonography of focal lesions of the skin and subcutaneous tissue.," *J. Ultrasound Med.*, vol. 18, no. 2, pp. 89–93, Feb. 1999.

[50] P. Giavedoni, L. Aranibar, and X. Wortsman, "Colour Doppler ultrasound early diagnoses simulator of proliferative nodule in congenital melanocytic nevus," *J. Eur. Acad. Dermatology Venereol.*, Apr. 2017.

[51] M. Bouer, A. I. Rodriguez-Bandera, F. Albizuri-Prado, A. Lobos, W. Gubeling, and X. Wortsman, "Real-time high-frequency colour Doppler ultrasound detection of cutaneous *Dermatobia hominis* myiasis," *J. Eur. Acad. Dermatology Venereol.*, vol. 30, no. 12, pp. e180–e181, Dec. 2016.

[52] X. Wortsman, A. Castro, and A. Figueroa, "Color Doppler ultrasound assessment of morphology and types of fistulous tracts in hidradenitis suppurativa (HS)," *J. Am. Acad. Dermatol.*, vol. 75, no. 4, pp. 760–767, Oct. 2016.

[53] C. (Christopher) Griffiths, J. Barker, T. Bleiker, R. (Robert J. G. . Chalmers, and D. Creamer, *Rook's textbook of dermatology*. .

[54] J.-L. Gennisson *et al.*, "Assessment of elastic parameters of human skin using dynamic elastography," *IEEE Trans. Ultrason. Ferroelectr. Freq. Control*, vol. 51, no. 8, pp. 980–989, Aug. 2004.

[55] W. Kim, S. G. Chung, T. W. Kim, and K. S. Seo, "Measurement of soft tissue compliance with pressure using ultrasonography.," *Lymphology*, vol. 41, no. 4, pp. 167–77, 2008.

[56] Thu-Mai Nguyen, M. Couade, J. Bercoff, and M. Tanter, "Assessment of viscous and elastic properties of sub-wavelength layered soft tissues using shear wave spectroscopy: Theoretical framework and in vitro experimental validation," *IEEE Trans. Ultrason. Ferroelectr. Freq. Control*, vol. 58, no. 11, pp. 2305–2315, Nov. 2011.

[57] X. Xiang *et al.*, "Quantitative Assessment of Healthy Skin Elasticity: Reliability and Feasibility of Shear Wave Elastography," *Ultrasound Med. Biol.*, vol. 43, no. 2, pp. 445–452, Feb. 2017.

[58] L. Wang, F. Yan, Y. Yang, X. Xiang, and L. Qiu, "Quantitative Assessment of Skin Stiffness in Localized Scleroderma Using Ultrasound Shear-Wave Elastography," *Ultrasound Med. Biol.*, vol. 43, no. 7, pp. 1339–1347, Jul. 2017.

[59] P. Mettler, J. Schroder, and C. Kleinmuntz, "Use of High Frequency Shear Wave™ Elastography (HFSWE) to identify and evaluate treatment of fascial adhesions," *J. Bodyw. Mov. Ther.*, vol. 19, no. 4, p. 678, Oct. 2015.

[60] A. R. Tilley and Henry Dreyfuss Associates., *The measure of man and woman : human factors in design*. Wiley, 2002.

[61] S. Bianchi, C. Martinoli, and I. F. Abdelwahab, "High-frequency ultrasound examination of the wrist and hand," *Skeletal Radiol.*, vol. 28, no. 3, pp. 121–129, Mar. 1999.

[62] I. Schoffl *et al.*, "DIAGNOSIS OF COMPLEX PULLEY RUPTURES USING ULTRASOUND IN CADAVER MODELS," *World Fed. Ultrasound Med. Biol.*, 2016.

[63] I. Tinazzi, A. Marchetta, D. Chessa, D. M. Gonagle, and P. Macchioni, "SAT0454 Finger flexor tendon pulley complex involvement in psa: an high resolution ultrasonographic

study," *Ann. Rheum. Dis.*, vol. 76, no. Suppl 2, pp. 945–945, Jun. 2017.
[64] M. H. Mozaffari and W.-S. Lee, "Freehand 3-D Ultrasound Imaging: A Systematic Review," *Ultrasound Med. Biol.*, vol. 43, no. 10, pp. 2099–2124, Oct. 2017.
[65] F. Padilla *et al.*, "Breast mass characterization using 3-dimensional automated ultrasound as an adjunct to digital breast tomosynthesis: a pilot study.," *J. Ultrasound Med.*, vol. 32, no. 1, pp. 93–104, Jan. 2013.
[66] E. West, O. Roy, and S. Schmidt, "Method and system for imaging a volume of tissue with tissue boundary detection," 30-Aug-2013.
[67] N. Duric *et al.*, "Breast imaging with the SoftVue imaging system: first results," 2013, vol. 8675, p. 86750K.
[68] L. O. Olsen, H. Takiwaki, and J. Serup, "High-frequency ultrasound characterization of normal skin. Skin thickness and echographic density of 22 anatomical sites," *Ski. Res. Technol.*, vol. 1, no. 2, pp. 74–80, May 1995.
[69] J. Sousa-Neves, M. Cerqueira, D. Santos-Faria, C. Afonso, and F. Teixeira, "Ultrasound assessment of skin thickness performed on fingers: a tool for estimating overall severity of skin disease in Systemic Sclerosis patients?," *Acta Reumatol. Port.*, Sep. 2017.
[70] S.-Y. Sun, "Ultrasound probe localization by tracking skin features," Massachusetts Institute of Technology, 2014.
[71] A. H. Slocum, *Precision machine design*. Prentice Hall, 1992.
[72] A. H. Slocum, *Precision machine design*. Prentice Hall, 1992.
[73] "Buy Free Form® SCULPT High Density Epoxy Dough-Crystalline Silica Free from Reynolds Advanced Materials." [Online]. Available: https://www.reynoldsam.com/product/free-form-sculpt/. [Accessed: 19-Aug-2018].
[74] P. A. Yushkevich *et al.*, "User-guided 3D active contour segmentation of anatomical structures: Significantly improved efficiency and reliability," *Neuroimage*, vol. 31, no. 3, pp. 1116–1128, Jul. 2006.
[75] D. M. Catarious, A. H. Baydush, and C. E. Floyd, "Characterization of difference of Gaussian filters in the detection of mammographic regions," *Med. Phys.*, vol. 33, no. 11, pp. 4104–4114, Oct. 2006.
[76] A. Summerfield and M. E. Ricklin, "The immunology of the porcine skin and its value as a model for human skin," *Mol. Immunol.*, vol. 66, no. 1, pp. 14–21, Jul. 2015.
[77] N. B. Purohit and L. J. King, "Ultrasound of lower limb sports injuries.," *Ultrasound*, vol. 23, no. 3, pp. 149–57, Aug. 2015.
[78] P. Robinson, "Sonography of Common Tendon Injuries," *Am. J. Roentgenol.*, vol. 193, no. 3, pp. 607–618, Sep. 2009.

APPENDICES

Appendix A: Error Analysis

The Z leadscrew is modeled as a cantilevered beam (Equation A.1) with a ring cross section (Equation A.2), loaded with drag from the water due to the motion of the probe (Equation A.3). The calculations for Z leadscrew deflection are shown in Table 7.1.

$$\delta = \frac{PL^3}{4EI} \quad (A.1)$$

$$I = (r_2{}^4 - r_1{}^4)\frac{\pi}{2} \quad (A.2)$$

$$P = F_d = \frac{1}{2}\rho v^2 C_d A \quad (A.3)$$

The X leadscrew is modeled as a beam fixed on both ends (Equation A.4), rather than a pinned beam, with a ring cross section (as above, Equation A.2), loaded with the weight of the Z carriage (Equation A.5). The calculations for X leadscrew deflection are shown in Table 7.2.

$$\delta = \frac{PL^3}{24EI} \quad (A.4)$$

$$P = mg \quad (A.5)$$

The deflection of the frame results in a small deflection of the probe downward. The calculations of error due to frame deflection are shown in Table 7.3.

$$\delta = L - L\cos\theta \quad (A.6)$$

$$\theta = \sin^{-1}\frac{\delta_{flex}}{2L} \quad (A.7)$$

The stepper motors have an associated error of 5%. Error is calculated as 5% of the travel (Equation A.8). The calculations of leadscrew error are shown in Table 7.4.

$$\delta = 0.05x \quad (A.8)$$

Table 7.1: Calculation of Z leadscrew deflection

Z leadscrew			
Variable	**Value**	**Units**	**Explanation**
Deflection $\delta = \frac{PL^3}{4EI}$	0.000214	mm	Cantilevered beam (from probe attachment)
Drag force $P = F_d = \frac{1}{2}\rho v^2 C_d A$	0.0756	N	Drag force from cross section of probe & speed
Density of water ρ	0.000000997	kg/mm^3	
Velocity of probe v	6.67	mm/s	
Drag coefficient C_d	1.05	Dimensionless	Conservative model as cube
Cross sectional area $A = bh$	3250	mm^2	
Base, width of probe b	65	mm	
Height submerged h	50	mm	Conservative estimation for submersion
Length of leadscrew L	145	mm	
Elastic Modulus E	180000	N/mm^2	Steel
Area moment of Inertia $I = (r_2{}^4 - r_1{}^4)\frac{\pi}{2}$	199	mm^4	
Outer radius of leadscrew r_2	6	mm	
Inner radius of leadscrew r_2	2.25	mm	

Table 7.2: Calculation of X leadscrew deflection

X leadscrew			
Deflection $\delta = \frac{PL^3}{24EI}$	0.0352	mm	Fixed/fixed
Deflection $\delta = \frac{PL^3}{4EI}$	0.211	mm	Pinned/pinned
Load $P = mg$	11.04	N	Load from weight of Z assembly, split between two rails
Length of leadscrew L	445	mm	
Elastic Modulus E	180000	N/mm^2	Steel
Area moment of Inertia $I = (r_2{}^4 - r_1{}^4)\frac{\pi}{2}$	6393	mm^4	
Outer radius of leadscrew r_2	8	mm	
Inner radius of leadscrew r_2	2.25	mm	

Table 7.3: Probe error from flex in frame

Flex in frame			
Delta at probe, z	0.00993	mm	
Delta at probe, x	3	mm	
Delta at base	6	mm	Experimental estimate
L	453	mm	
Theta	0.00662	radians	

Table 7.4: Error due to stepper motor accuracy

Stepper motor accuracy			
Delta between images, X	0.011724557	mm	
Delta between images, Z	0.002063522	mm	
Delta from end to end, X	6.25	mm	
Delta from end to end, Z	1.1	mm	
Travel between image, X	0.234491137	mm	
Travel between image, Z	0.04127044	mm	
Max travel, X	125	mm	
Max travel, Z	22	mm	
Frame rate	28	Hz	
Speed	6.67	mm/s	
Step accuracy	0.05	5%	

Appendix B: Data Gathering Procedures

1. Tank should be filled at least 10 minutes before scanning to allow bubbles to release.
2. Power up the CNC and plug the Arduino in to the computer.
3. Power up the ultrasound machine and input patient data.
4. Start with a flash drive with a clear DICOMDIR folder, so the numbering in saved files is consistent with the numbers displayed on the ultrasound machine.
5. Start Universal GCode Sender, and confirm the paths are set correctly. The paths are shown below in Table 7.5.
6. Position the armrest for the view of the arm to be used for the first scan. Move the probe holder to the center of the armrest.
7. Have subject read IRB information and fill out consent form.
8. Using the form on the following page, record the name of the subject, the time, and the goal of the scan.
9. Without the probe in place move the CNC in X to the middle of the armrest when angled to the designed side.
10. Instruct the subject to place their hand on the armrest, positioning the pegs for maximum comfort and compliance.
11. Move the CNC in Y over the arm's highest point when angled, around the third knuckle (dorsal imaging) or thumb pad (ventral imaging)
12. Place the zeroing tool on the probe holder, and lower it incrementally until just touching the surface of the arm. Set the current position with the values for the center of the path.
13. Allow the subject to move their arm, constrain the probe in the probe holder.
14. Instruct the subject to place their arm and hold still. Begin scanning from the back right, and continue scanning until the upper arm creates a barrier. Record the approximate location of each scan on the arm using the worksheet shown on the following page.
15. Allow the subject to relax and remove and dry their arm.
16. Export and save all data from ultrasound machine to USB

Table 7.5: Ultrasound paths

Armrest angled right	Armrest angled right	Armrest angled left
Starting position	G1 X125 Z0 F400	G1 X154 Z22 F400
Right to left	G1 X63 Z11 F400 G1 X0 Z22 F400	G1 X91 Z11 F400 G1 X28 Z0 F400
Left to right	G1 X63 Z11 F400 G1 X125 Z0 F400	G1 X91 Z11 F400 G1 X154 Z22 F400

Name: _____

Date: _____

Time: _____

Scan description:

_____

_____

Number each scan location on arm with the # scan saved by the ultrasound machine.

Dorsal (top) of arms:

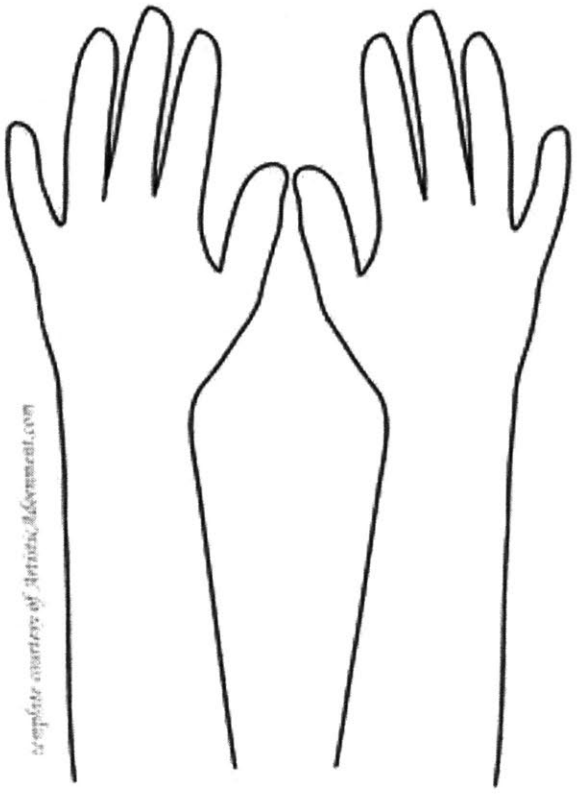

Ventral (bottom) of arms:

https://i.pinimg.com/236x/fc/53/0c/fc530c771dc7ec76b1a6d0c901fe1e4f--how-to-blog-henna-tattoo-designs.jpg